

NWRA-BeCR-05-R305

17 August 2005

Laboratory and Numerical Studies of the Effects of Shear on 3-D Vortex Evolution

Final Report for
ONR Contract N00014-01-C-0316

By

Donald P. Delisi
and
Robert E. Robins

For

Dr. Ronald Joslin
Office of Naval Research

DISTRIBUTION STATEMENT A
Approved for Public Release
Distribution Unlimited

508 NE 20th Street, Bellevue, WA 98007-3713

Tel: 425.644.9660 Fax: 425.644.8422

6 September 2005

Office of Naval Research
Attn: Dr. Ronald D. Joslin, ONR Code 333
Ballston Tower One
800 North Quincy St.
Arlington, VA 22217-5660

REF: N00014-01-C-0316

RE: Transmittal of Final Report, NWRA-BeCR-05-R305

Enclosed is the final report for the above referenced contract. This report, entitled "Laboratory and Numerical Studies of the Effects of Shear on 3-D Vortex Evolution," is by Dr. Donald Delisi and submitted as required by Data Item A002.

The DD Form 250 is also enclosed for acceptance of the report as the final deliverable required by the contract. Please return a signed copy of the DD Form 250 in the enclosed self-addressed envelope.

For technical questions, please contact Dr. Delisi at (425) 644-9660 ext. 307 or by e-mail at don@nwra.com. For contractual issues, I can be reached at (425) 644-9660 ext. 220 or by e-mail at yvonne@nwra.com.


Yvonne Pipkin

Contracts Administrator

YP:sb

enc.

cc: Director, NRL - Attn: Code 5227 (1 copy)
DCMA Seattle – Attn: Bill Miner (letter only)
DTIC/OCA (2 copies)

Contents

1. Introduction.....	1
2. The Laboratory Facility and Shear Hardware.....	1
3. The Numerical Model	9
4. Theoretical Considerations	11
5. Results.....	12
5.1 Case with Linear Shear	12
5.2 Case with $V'' > 0$	15
5.3 Case with $V'' < 0$	18
5.4 Case with Mixed Shear	21
5.5 Laboratory Measurements of Vortex Evolution through a Sharp Jump in Shear Gradient.....	24
5.6 3-D Numerical Simulations	30
5.6.1 Previous Laboratory Measurements	31
5.6.2 3-D Numerical Simulations	33
6. Summary.....	38
REFERENCES	40

List of Figures

Figure 1. Photograph of the wing used to generate vortices in the laboratory experiments	2
Figure 2. Measured coefficient of lift vs. angle of attack for the wing used in the laboratory experiments.....	3
Figure 3. A schematic drawing of the cross-track view of a vortex cell, containing a counter rotating vortex pair, migrating downward.	3
Figure 4. View of the shear assemblies looking up the towing tank.	4
Figure 5. View of the shear assemblies looking into the test section from the side.	5
Figure 6. View of the shear assemblies looking directly into the test section from the side.	6
Figure 7. Measured flow rates through one pipe/nozzle assembly.....	7
Figure 8. Measurements of linear shear in the towing tank.	8
Figure 9. Measurements of linear shear in the towing tank with time after the start of the run.	9
Figure 10. Example of equation (3) in the text.	12
Figure 11. Velocity profile for the case for vortex evolution with linear shear.....	13
Figure 12. Vortex trajectories for the linear shear case.	14
Figure 13. Measurements of the angle of tilt of the line joining the vortex cores for the linear shear case.	15
Figure 14. Velocity profile for the case for vortex evolution with $V''>0$	16
Figure 15. Vortex trajectories for the case with $V''>0$	17
Figure 16. Measurements of the angle of tilt of the line joining the vortex cores for the $V''>0$ case.....	18
Figure 17. Velocity profile for the case for vortex evolution with $V''<0$	19
Figure 18. Vortex trajectories for the case with $V''<0$	20
Figure 19. Measurements of the angle of tilt of the line joining the vortex cores for the $V''<0$ case.....	21
Figure 20. Velocity profile for the case with mixed shear ($V''>0$ and $V''<0$).	22
Figure 21. Vortex trajectories for the case with mixed shear.	23
Figure 22. Measurements of the angle of tilt for the case with mixed shear.	24
Figure 23. Velocity profile for the case with sharp vertical gradients of shear.	25
Figure 24. Similar to Figure 23 with the addition of the vortex cell.	26
Figure 25. Laboratory measurements of vortex trajectories for the case with sharp vertical gradients of shear.....	27

Figure 26. The angle of tilt of the vortex cores for the case with sharp vertical gradients of shear along with the laboratory measurements of the velocity profile from Figure 23	28
Figure 27. The angle of tilt of the vortex cores for the case with sharp vertical gradients of shear for a towing speed of 160 cm/sec and for a towing speed of 80 cm/sec.	29
Figure 28. Laboratory measurements of the peak-to-peak vertical amplitude of two-dimensional line vortices generated from a wing as a function of nondimensional time for suns with varying amounts of ambient turbulence. .	32
Figure 29. Similar to Figure 28 with the addition of the 3-D numerical predictions for the case with no ambient turbulence and no ambient shear.....	33
Figure 30. Similar to Figure 29 with the addition of the 3-D numerical predictions for the case with ambient turbulence and no ambient shear and the case with ambient turbulence and ambient shear.....	34
Figure 31. H vs T plot for the three 3-D numerical simulations.....	36
Figure 32. Numerical model results for the no turbulence no shear case turbulence, no shear case and turbulence and shear case for T=2, T=3, T=4 and T=5.	37

1. Introduction

This report documents the results of ONR Contract N00014-01-C-0316. The goal of this study was to begin to understand the effects of vertical shear on the evolution of a vortex pair.

Vorticity is always generated from a three-dimensional lifting surface. Behind this surface, the vorticity typically rolls up quickly into a pair of counter-rotating vortices. Since vortices transport mass and momentum, their evolution and persistence are important in naval hydrodynamics.

It is well known that the ambient background has a significant effect on vortex evolution. While many background effects have been studied for their effect on vortex evolution, several important, realistic effects have not yet been intensely studied.

We believe the most glaring of these gaps in our understanding is the lack of inclusion of the effect of ambient shear. The Richardson number, R_i , is defined as

$$R_i = N^2 / (dU/dz)^2 , \quad (1)$$

where N is the Brunt-Vaisala frequency, defined as $N = (-g/\rho d\rho/dz)^{1/2}$, where ρ is density, g is the acceleration due to gravity, U is the horizontal speed of the fluid, and z is the vertical coordinate. Thus, the Richardson number is a ratio of buoyancy (stratification) effects to inertial (or shear) effects. It is well established that R_i is commonly of order one in the ocean. The importance of R_i being of order unity is that the effects of shear should be as important as the effects of stratification.

In this study, we investigated the effects of vertical shear on the evolution of vortices from a lifting wing. We believe it is essential to include the effects of shear if we are to fully understand vortex evolution in the ocean. We also note that shears are larger in the littoral region than in the open ocean. Thus, to fully understand vortex evolution in the littoral, we must understand the effects of shear on vortex evolution.

2. The Laboratory Facility and Shear Hardware

In the laboratory part of this study, we used wings in our towing tank to generate the vortex pairs. As a lifting wing is towed down the tank, the wing generates a vortex pair that migrates downward, towards the floor of the tank. The experiments were performed in the NorthWest Research Associates (NWRA) towing tank. This towing tank measures 10 m long, 1 m wide, and 1 m deep. The wing was a curved, flat plate, and had a span of 2 inches and a chord of 1 inch (Figure 1). The measured coefficient of lift vs. angle of attack ($C_L-\alpha$) curve for this wing is shown in Figure 2. For the measurements reported here, the wing was towed down the tank at an angle of attack of 13 degrees at speeds ranging from 80 to 160 cm/s.

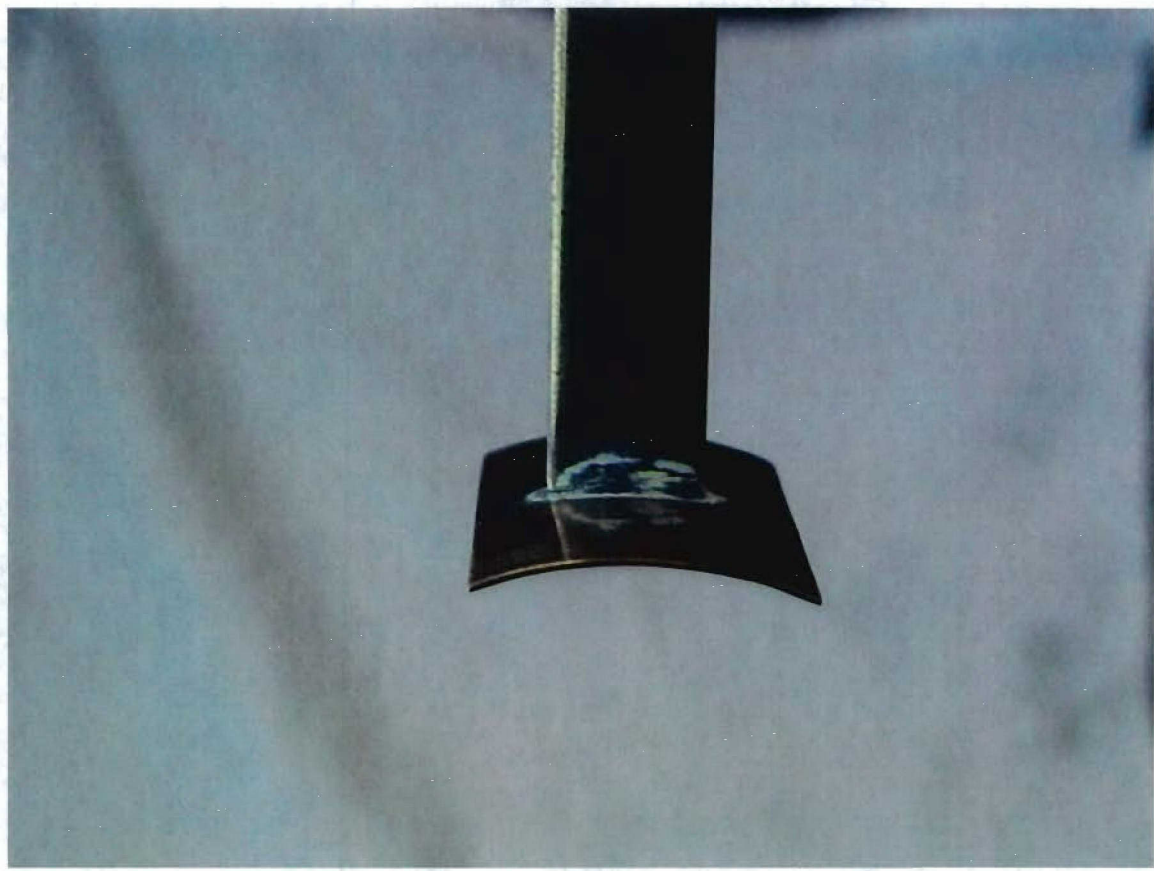


Figure 1. Photograph of the wing used to generate vortices in the laboratory experiments.

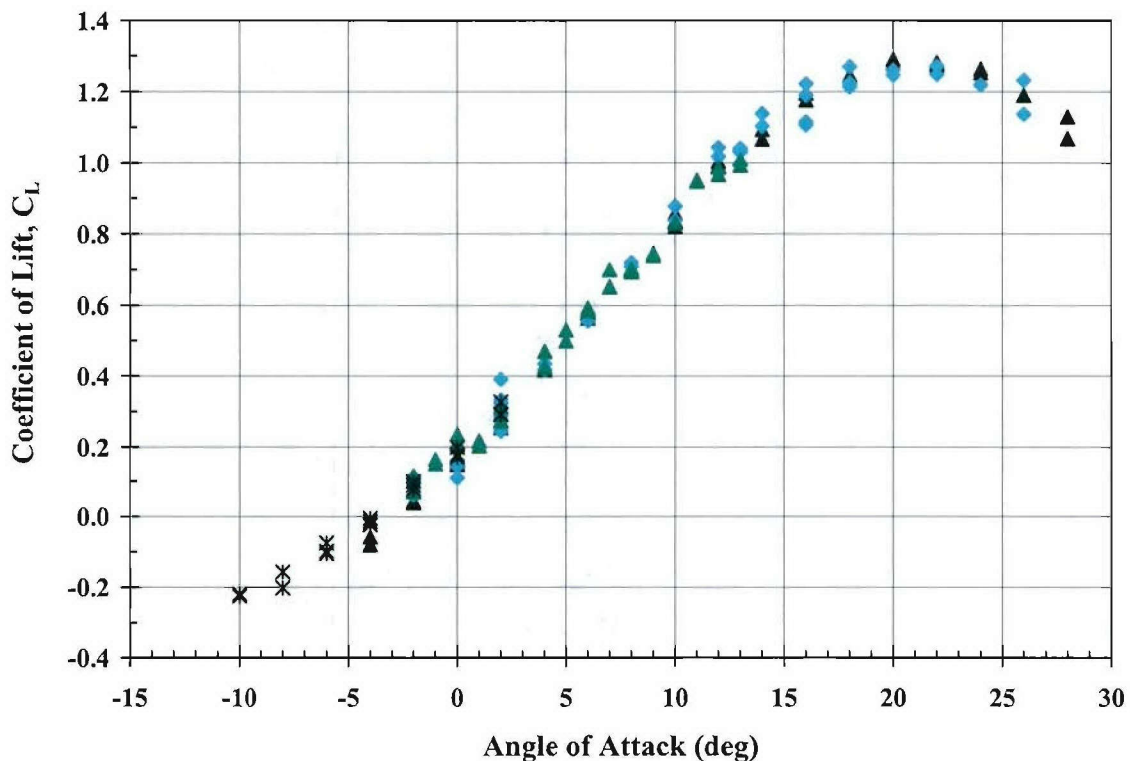


Figure 2. Measured coefficient of lift vs. angle of attack for the wing used in the laboratory experiments.

A counter-rotating vortex pair consists of two vortex cores surrounded by turbulent fluid in the vortex cell. Figure 3 shows a schematic drawing of the cross-track view of such a counter rotating vortex pair, migrating downward. A vertical shear is shown in the cross-track direction. In this case, the cross track shear is linear with height.

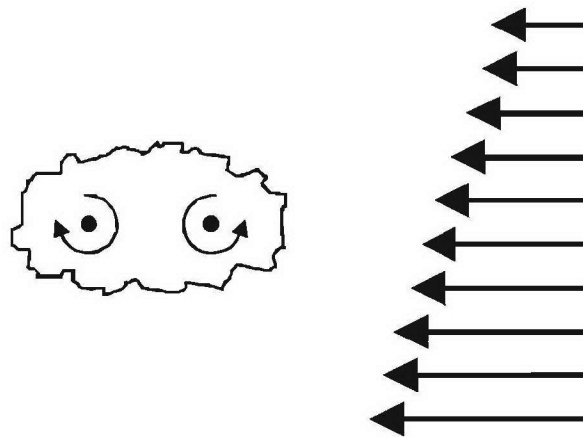


Figure 3. A schematic drawing of the cross-track view of a vortex cell, containing a counter rotating vortex pair, migrating downward. A vertical shear is shown in the cross-track direction. In this case, the cross track shear is linear with height.

Our goal was to study the effects of cross-track shear on the evolution of the vortices generated by our wing. In order to study this effect, we had to be able to generate a stable, constant shear flow in the laboratory tank in the cross-track direction. Since the wing is towed down the long axis of our towing tank, we had to set up the shear hardware to produce a shear from sidewall to sidewall (i.e., in the cross-track direction). To produce this shear, we had to produce a uniform, but different, velocity in many vertical layers in the tank, as illustrated in Figure 3. At each depth in the tank, we designed a horizontal pipe and nozzle to generate a layer of flow moving horizontally at a prescribed velocity. The requirement was for each pipe/nozzle (i.e., shear) assembly to produce a nearly constant velocity layer along its length, which was ~ 1 m.

Figures 4 to 6 show photographs of the shear hardware. Figure 4 shows a view of the shear assemblies looking up the towing tank. The pipe/nozzle assemblies are located on the sidewalls of the towing tank. The direction of the wing is out of the page. The arrow shows the direction of the velocities from the shear nozzles. These directions are perpendicular to the direction of the wing, and, therefore, are in the cross track direction of the vortices.

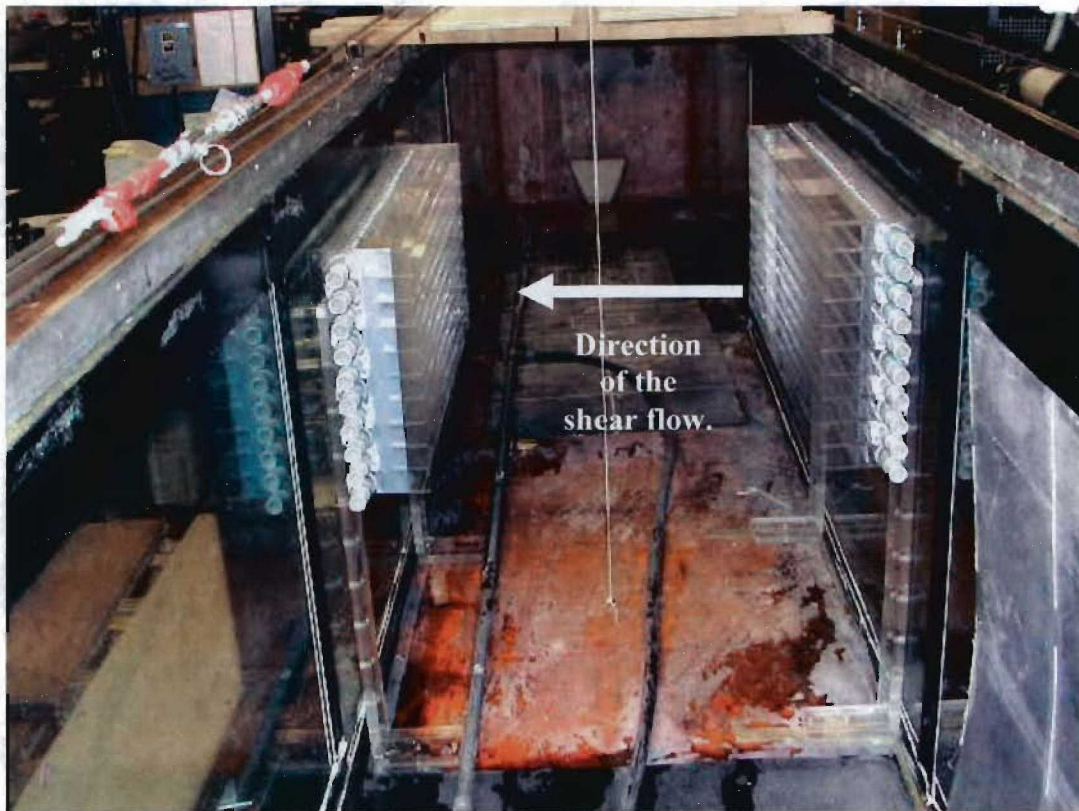


Figure 4. View of the shear assemblies looking up the towing tank. The assemblies are located on the sidewalls of the towing tank. The direction of the wing is out of the page. The arrow shows the direction of the velocities from the shear nozzles. These directions are perpendicular to the direction of the wing, and, therefore, are in the cross track direction of the vortices.

Figure 5 is a photograph of the shear assemblies looking into the test section from the side. The shear assemblies cover a horizontal distance of ~1 m along the test section, in the direction of travel of the wing, and they cover approximately the upper half of the tank. (Each assembly has a vertical height of 1.5 inches, and there are ten assemblies, and, hence, ten fluid layers.) In this photograph, the connection hoses are connected only to the assemblies on the far wall of the test section, which are used for suction. The assemblies on the wall closest to the camera are used for supplying the fluid. In the bottom right of the photograph are the pumps which supply the fluid to the discharge assemblies and collect the fluid from the suction assemblies.



Figure 5. View of the shear assemblies looking into the test section from the side. The assemblies are located on the sidewalls of the towing tank. The shear assemblies cover a distance of ~1 m along the test section, in the direction of the wing, and they cover about the upper half of the tank. In this picture, the connection hoses are connected only to the nozzles on the far wall of the test section. The nozzles on the back wall are the suction nozzles. The nozzles on the wall closest to the camera are the discharge nozzles. In the bottom right of the photograph are the pumps which supply the fluid to the discharge nozzles and collect the fluid from the suction nozzles.

Figure 6 is a photograph of the shear assemblies looking directly into the test section from the side of the towing tank. In this view, the wing is towed from right to left. The shear assemblies cover a distance of ~1 m along the test section, in the direction of the wing, and they cover about the upper half of the tank (~0.5m). The pumps which supply the fluid to the discharge assemblies (seen here) and collect the fluid from the suction assemblies (the far wall, which cannot be seen here) are seen in the bottom part of the photograph.

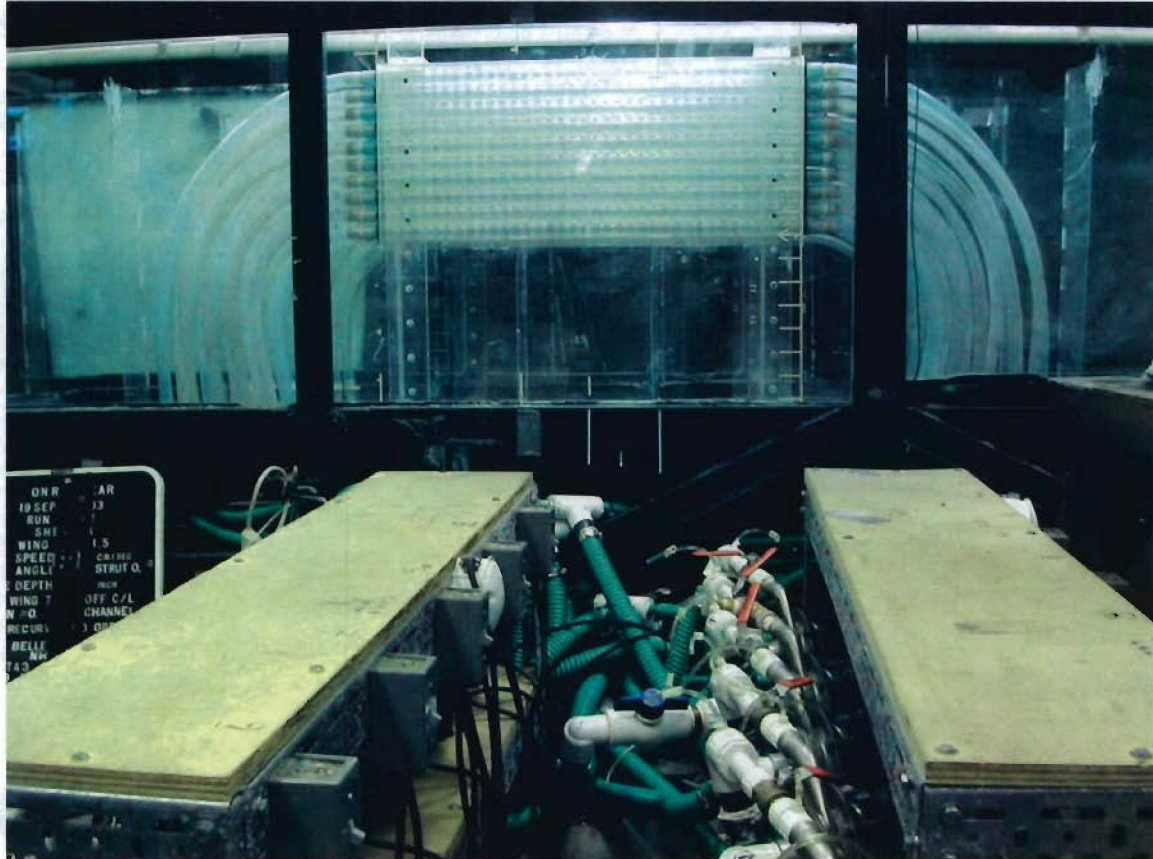


Figure 6. View of the shear assemblies looking directly into the test section from the side. In this view, the wing is towed from right to left. The shear assemblies cover a distance of ~1 m along the test section, in the direction of the wing, and they cover about the upper half of the tank. The pumps which supply the fluid to the discharge nozzles (the far wall which cannot be seen here) and collect the fluid from the suction nozzles (on the near wall) are seen in the bottom part of the photograph.

Three hardware design questions that needed to be answered early in the study were the following:

- Could the nozzles generate a uniform velocity flow in the horizontal direction?
- Could we generate a reproducible shear flow? and

- c. Could we generate a shear flow that would persist for a long enough time that an experiment could be performed?

The first of these questions is answered in Figure 7. In this figure, we show the measured flow rate out of one pipe/nozzle assembly for three different flow rates, as a function of distance along the assembly. In the towing tank, each nozzle is 36 inches long and has incoming water on both ends. The figure shows data from one end of the nozzle to the centerline of the nozzle. The importance of Figure 7 is that it shows nearly constant flow along the pipe for three different flow rates. Thus, each nozzle generates a nearly constant velocity layer horizontally along the tank.

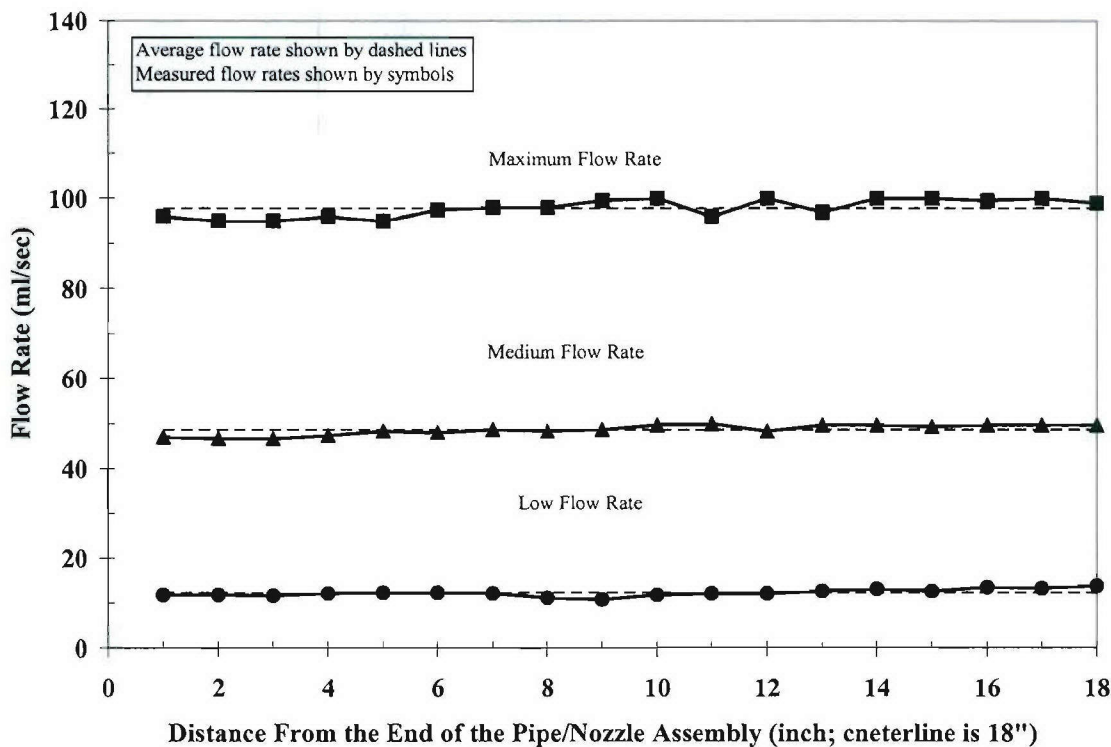


Figure 7. Measured flow rates through one pipe/nozzle assembly. The assembly is 36 inches long, and is fed with water from both ends. This figure shows nearly constant flow rate out of the nozzle for three different flow rates.

To measure the fluid velocities in the tank, and, hence, the vertical shears, we placed small, neutrally buoyant particles in the flow. To measure the motions of the particles, we placed a small mirror in the tank and recorded the flow, including the particles, with a video camera. Using a frame grabber and knowing the video frame rate of 30 fps, we could measure the horizontal speeds of the particles. Figure 8 shows results for two nominally similar runs where we tried to set up a linear shear in the towing tank. For these runs, the cross track shear flow was started and allowed to stabilize. Once stabilized, the particle motions were followed for ten seconds.

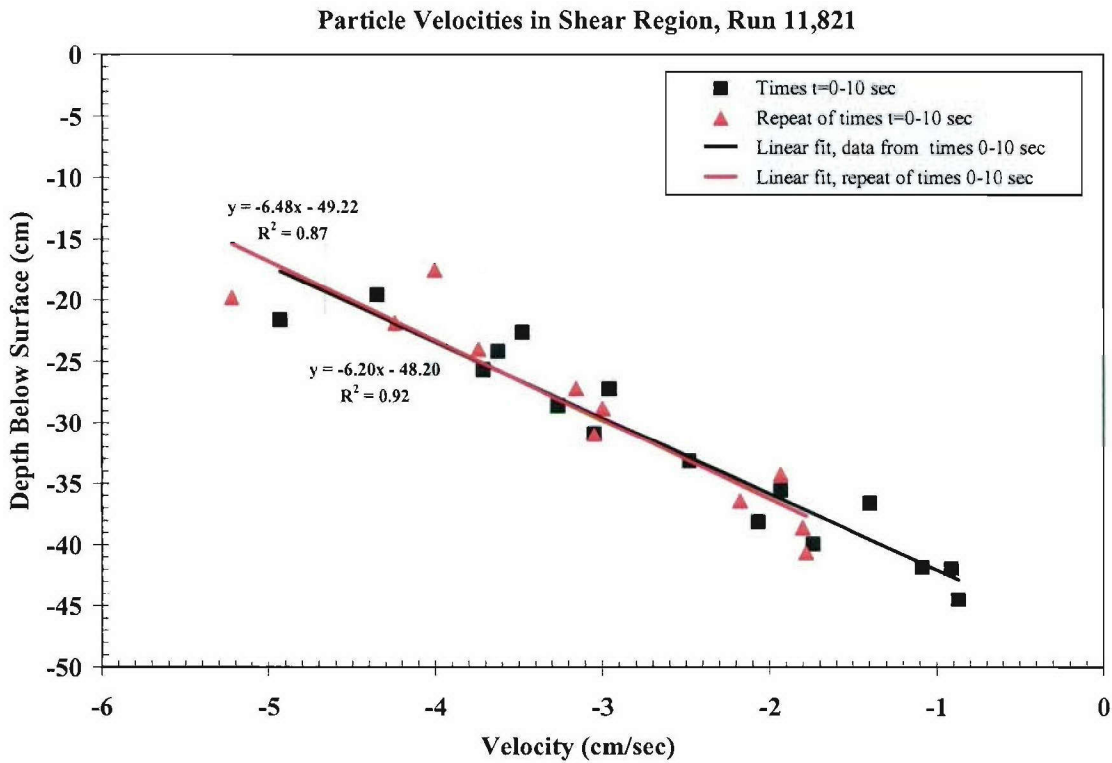


Figure 8. Measurements of linear shear in the towing tank. Squares show the shear immediately after a stable flow develops. Triangles show the shear at the same time in a nominally similar run. The lines are least square linear fits through the data. These results show that the shear is repeatable from run to run.

The nominal shear flows in Figure 8 were linear with depth. The black squares show the velocities at the start of one run, after a stable flow develops, and the red triangles show the velocities at the start of a nominally similar run. The straight lines are the linear least squares fits through the data. The slopes of these lines are different by around 4.5%. This nearly identical linear shear between these two runs indicates that the shear flows are adequately reproducible.

Measurements like those shown in Figure 8 were taken at successive times after the flow was developed, and the results are shown in Figure 9. The two data points at $t = 5$ sec in Figure 9 are the data from Figure 8. Figure 9 shows that the shear stays approximately constant with time over the first two minutes of the run.

Taken together, Figures 7 to 9 show that the nozzles generate a uniform flow in the horizontal direction and that we are able to generate a reproducible shear flow that persists for long enough to run an experiment.

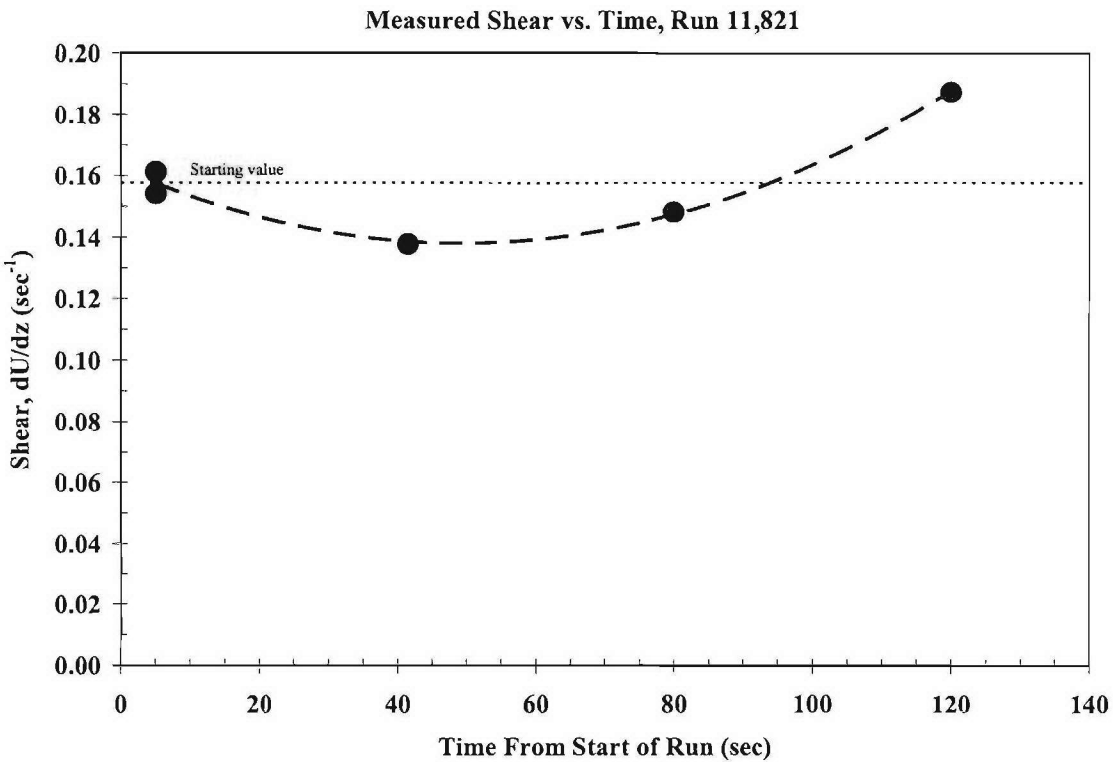


Figure 9. Measurements of linear shear in the towing tank with time after the start of the run. This figure shows that the shear stays approximately constant over the first 2 minutes of the run.

3. The Numerical Model

For the numerical studies, we used a three-dimensional (3-D) incompressible LES Navier-Stokes solver to study the effects of shear on the evolution of trailing vortices. A key feature of the numerical approach was that the traditional LES formulation was modified so that subgrid dissipation was damped in regions of intense rotation, such as the core of each vortex. The result was that trailing vortex cores remained tight throughout their evolution, in agreement with both laboratory and full-scale observations.

To briefly summarize the numerical formulation, the equations solved are the incompressible Navier-Stokes equations with a modified Smagorinsky subgrid formulation (described by Holzapfel (2004)) that allows vertically varying ambient current and density. The modification to the Smagorinsky subgrid scale formulation is simply that eddy viscosity is multiplied by the factor $1/(1+\alpha R_{ir})$, where R_{ir} is a rotational Richardson number based on flow curvature. In this formulation, α is usually set to 1; R_{ir} goes to zero for straight flow and becomes large for highly curved flow. Thus, the eddy dissipation goes to zero in the highly rotational vortex cores. This zero eddy

dissipation in the vortex cores keeps the cores tight and does not allow them to grow with time.

For our simulations, horizontal boundary conditions are periodic, and the boundary condition at the top and bottom of the computational domain is chosen to be open. Other possible choices to these conditions are rigid lid with either a no slip or a free slip specification. Horizontal derivatives are computed via FFT and vertical derivatives with a 6th order compact scheme. The time-stepping is 2nd order Adams-Bashforth, with a projection correction applied every time-step to ensure incompressibility. High wavenumber smoothing is periodically applied to maintain numerical stability. Horizontal smoothing is performed via FFT and vertical smoothing is performed with a compact scheme.

Simulations are initialized with a horizontal counter-rotating pair of vortices placed at a vertical level z_0 and separated by a nominal distance b_0 . For the 2-D calculations, we used a 2-D version of the 3-D model which ran much more quickly than the full 3-D code

For the 3-D calculations, we employed axial perturbations so the vortices would link via Crow instability (Robins and Delisi, 1997 and 1998; Delisi and Robins, 2000). More specifically, each vortex was formed from a superposition of component vortices having core radius r_C , with each component having a very low-amplitude sinusoidal axial variation, the wavenumber of the sinusoid being in the range between 1 and $N_x/2$, where N_x is the number of grid points in the axial direction. The circulation for the sinusoidal components varied as $k^{-5/6}$ (so that energy will vary as $k^{-5/3}$), where k is wavenumber and the total circulation for each superposition is Γ_0 , where Γ_0 is the total circulation of the vortex pair. The tangential velocity of each component varied as $r/(r^2+r_C^2)$, where r is distance from the vortex center.

In addition, there is provision for the fluid in which the vortices are embedded to be turbulent, with an initially specified eddy dissipation rate. This initial ambient turbulence was generated using the methods described by de Bruyn Kops and Riley (1998). Finally, when the ambient fluid is turbulent, there is a provision to increase the level of turbulence within the vortex cores to simulate the entrainment of turbulence resulting from the process of vortex generation.

As the evolution of the vortices proceeds, the vortices migrate vertically due to mutual induction, and instabilities due to the vortex formulation and the ambient turbulence develop, causing the vortices to eventually link and form rings which continue to migrate vertically. If the vortices were allowed to approach the top or bottom of the computational domain, the simulation would be stopped before the boundary affected the vortices, and the domain would be shifted to allow the vortices to propagate without interference.

4. Theoretical Considerations

The result of subtracting the z-differentiated y-momentum equation from the y-differentiated z-momentum equation, and using $\text{div}(V) = 0$ is:

$$0 = \frac{d}{dt} [\eta_x] - W\bar{V''} - \nu\nabla^2[\eta_x] - \frac{\partial U}{\partial x}(\eta_x - \bar{V'}) + \frac{\partial U}{\partial y}\frac{\partial W}{\partial x} - \frac{\partial U}{\partial z}\frac{\partial V}{\partial x} + \nu\bar{V'''} + \frac{g}{\rho_0}\frac{\partial \rho}{\partial y} \quad (1)$$

where $\eta = \text{vorticity} = \partial W / \partial y - \partial V / \partial z$, and W and V are the z and y velocity components.

If we assume 2-D flow ($U \equiv 0$), and neglect viscous and buoyancy effects, we get:

$$\frac{d}{dt} [\eta_x] = W\bar{V''}. \quad (2)$$

Integrating over a small area, A, surrounding a vortex gives:

$$\frac{d}{dt} \Gamma_A = \iint_A W\bar{V''} . \quad (3)$$

We use eqn. (3) to predict the tilting of the line connecting the vortex cores. Since W is positive up, and the laboratory (and numerical) vortices always propagate downward, W, for us, is always negative. Thus, if V'' is positive ($V'' > 0$), eqn. (3) says that $d\Gamma_A/dt$ will be negative.

An example of eqn. (3) is shown in Figure 10. In this example, $V'' < 0$. With the vortex pair on the left migrating downwards (in the negative direction), eqn. (3) says that $d\Gamma_A/dt > 0$. Thus, the right vortex (with $\Gamma > 0$) strengthens relative to the left vortex. This results in the line joining the vortex cores tilting in the counterclockwise direction. The result is a non-vertical migration of the vortex pair. Note that the sense of the shear is clockwise, but the line joining the vortex cores tilts in the counterclockwise direction. Thus, the tilt of the vortex cores is opposite to the sense of the shear, which is counterintuitive.

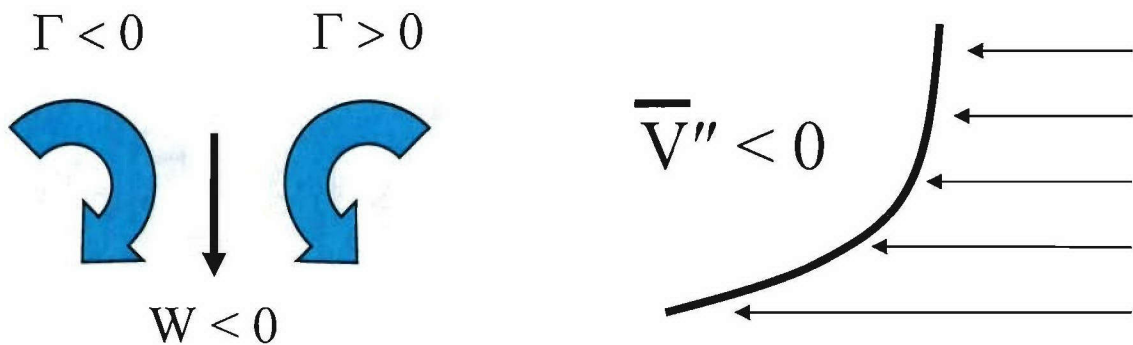


Figure 10. Example of equation (3) in the text. In this example, $V'' < 0$, where V is the horizontal velocity component. With the vortex pair shown on the left, $W < 0$ and eqn. (3) says that $d\Gamma_A/dt > 0$. Thus, the right vortex (with $\Gamma > 0$) strengthens since it gains a small positive increment relative to the left vortex, which also gains a small positive increment, thus losing a little strength. Thus, the line joining the vortex cores will tilt counterclockwise, opposite to the sense of the shear. The result is a non-vertical migration of the vortex pair.

In the above example, $V'' < 0$ and the line joining the vortex cores tilts in the counterclockwise direction. A similar example would show that, if V'' were positive, ($V'' > 0$), the tilt would be clockwise. Thus, for future reference,

$$\begin{array}{ll} V'' > 0 & \text{implies a clockwise tilt and} \\ V'' < 0 & \text{implies a counterclockwise tilt.} \end{array}$$

5. Results

5.1. Case with Linear Shear

With no shear, the vortices migrate vertically downward, with no tilt of the vortex cores.

With a linear shear, $V' = \text{constant}$, and $V'' = 0$. From eqn. (3), $d\Gamma_A/dt = 0$, and there should be no tilt of the vortex cores. Figure 11 shows the velocity profile for the case for vortex evolution with linear shear. The triangles show the measured laboratory velocities as a function of depth below the surface. The solid line is a linear, least squares fit to the laboratory data. The filled circle shows the starting depth of the laboratory wing generating the vortex pair. The short lines on the velocity axis at -5.5 show the depths of the shear nozzles which are generating the linear shear flow.

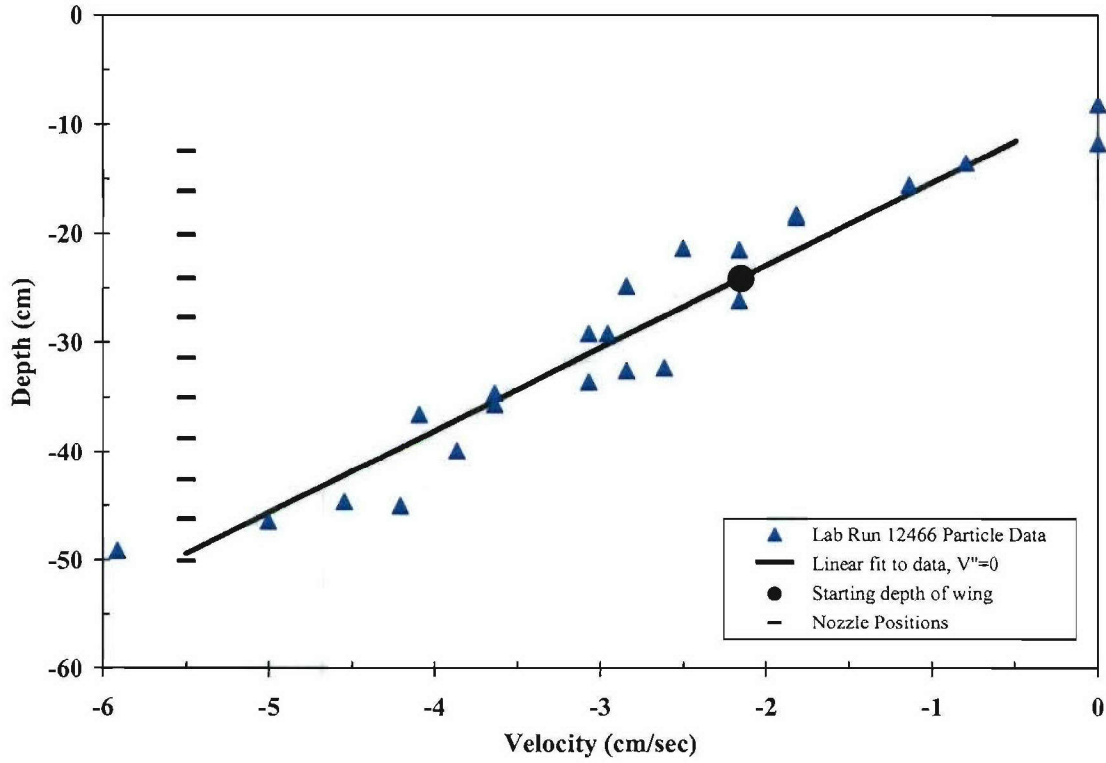


Figure 11. Velocity profile for the case for vortex evolution with linear shear. The triangles show the measured laboratory velocities as a function of depth below the surface. The solid line is a linear, least squares fit to the laboratory data. The filled circle shows the starting depth of the laboratory wing generating the vortex pair. The short lines on the velocity axis at -5.5 show the depths of the shear nozzles which are generating the linear shear flow.

Figure 12 shows vortex trajectories for the linear shear case shown in Figure 11. The blue diamonds in Figure 12 show the laboratory measurements vs. time, and the red squares show the corresponding numerical predictions using the laboratory measurements for wing depth, laboratory measurements for initial vortex descent velocity, laboratory measurements for initial vortex separation distance, and the linear velocity (shear) profile from Figure 11. The solid black line at a depth of -25 cm shows the depth of the trailing edge of the wing that generates the vortex pair. This is also the starting depth of the model predictions. The solid and dashed lines joining the measurements and predictions show the depths of the vortices at unit values of T , where T is nondimensional time and $T = V_o t$, where V_o is the initial descent velocity of the vortex pair and t is dimensional time. Note the following in Figure 12. First, the laboratory measurements and numerical predictions nearly overlay each other. This agreement is encouraging, since this is a simple flow, and suggests that we may have agreement for more complex flows. Second, the vertical transport is nearly linear with depth. This transport is expected, since the velocity profile is linear, but it confirms our expectations. Third, the blue solid lines and red dashed lines joining the left and right vortex positions at unit values of T nearly

overlay each other. This agreement shows that the temporal evolution of the laboratory measurements agrees very well with the temporal evolution of the numerical predictions. Finally, these blue solid and red dashed lines are very nearly horizontal, implying that there is essentially no tilt in the line joining the vortex cores.

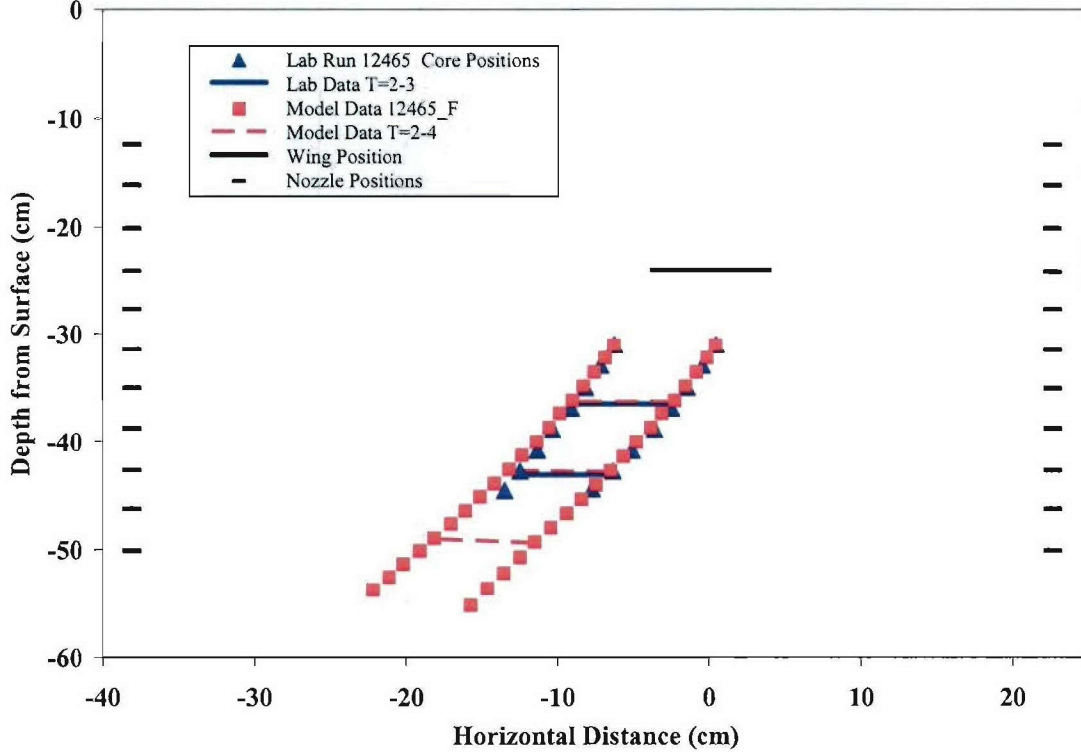


Figure 12. Vortex trajectories for the linear shear case. The blue diamonds show the laboratory measurements vs. time, and the red squares show the corresponding numerical predictions using the laboratory measurements for wing depth, initial vortex descent velocity, initial vortex separation distance, and velocity (shear) profile. The solid black line at a depth of -25 cm shows the depth of the trailing edge of the wing that generates the vortex pair. The positions of the shear nozzles are shown as short solid lines on each side of the plot. The solid and dashed lines joining the measurements and predictions show the depths of the vortices at unit values of T .

The tilt in the line joining the vortex cores is quantified in Figure 13. In this figure, the blue triangles are the laboratory measurements, and the red squares are the predictions from the numerical model. For the linear shear case, there is essentially no tilt of vortex cores for depths closer to the surface than around -45 cm. The small tilt angles below -45 cm are due to the end of the shear nozzles and the return of the flow to a zero velocity below ~ 50 cm depth (see the shear nozzle positions in Figure 11).

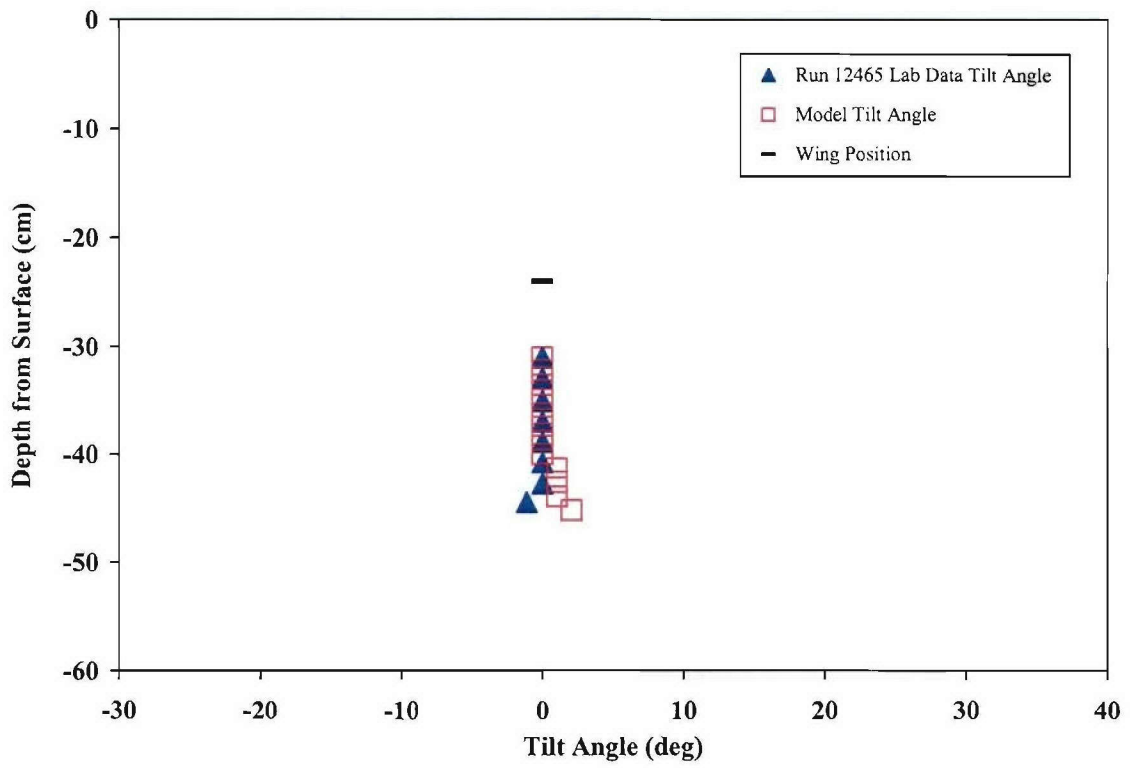


Figure 13. Measurements of the angle of tilt of the line joining the vortex cores for the linear shear case. The blue triangles are the laboratory measurements, and the red squares are the predictions from the numerical model. For the linear shear case, there is essentially no tilt of vortex cores.

The important point from Figures 11 to 13 is that there is no vortex tilt for a linear shear, as predicted by equation (3).

5.2. Case with $V'' > 0$

Figure 14 shows the velocity laboratory measurements (blue diamonds) for the case with $V'' > 0$. The curve through the measurements is a best fit to the data. The magenta line shows the parts of the curve where $V'' > 0$, and the green lines show the parts where $V'' < 0$. Again, the filled circle shows the starting depth of the laboratory wing generating the vortex pair. Note that this starting depth is within the region where $V'' > 0$.

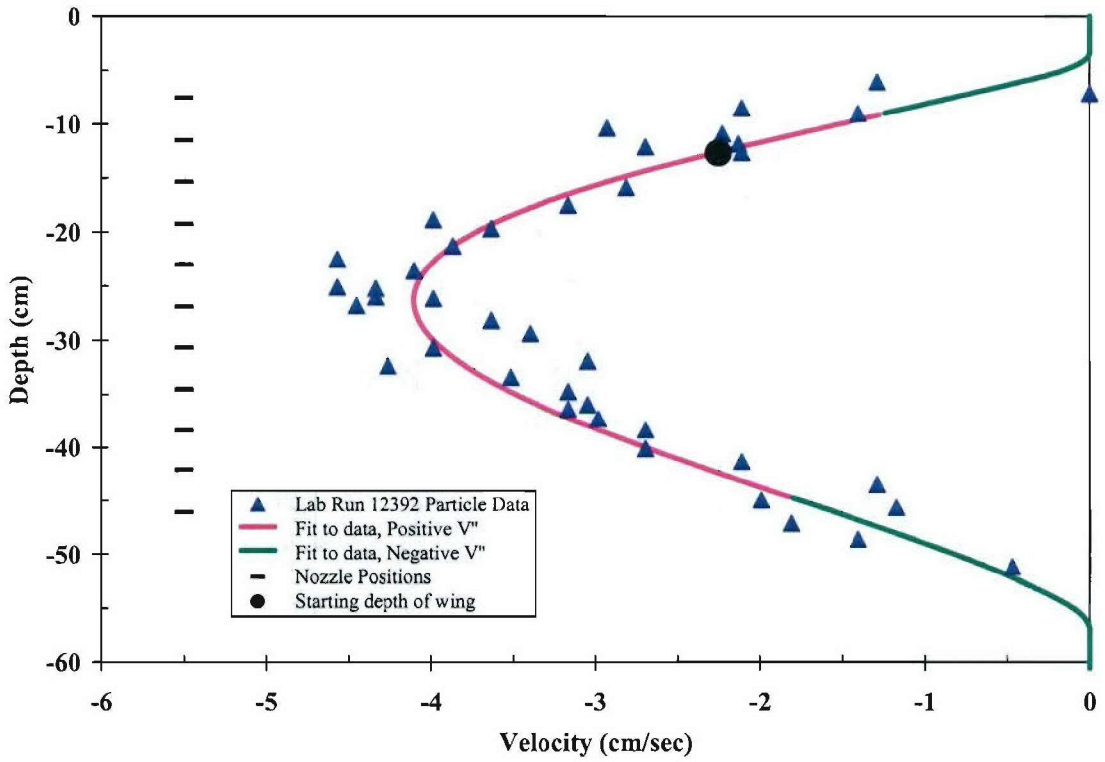


Figure 14. Velocity profile for the case for vortex evolution with $V'' > 0$. The triangles show the measured laboratory velocities as a function of depth below the surface. The curve through the measurements is a best fit to the data. The magenta line shows the part of the curve where $V'' > 0$, and the green lines show the parts where $V'' < 0$. The filled circle shows the starting depth of the laboratory wing generating the vortex pair. Note that this starting depth is within the region where $V'' > 0$.

From eqn. (3), for $V'' > 0$, we expect a clockwise tilt of the line joining the vortex cores. Figure 15 shows the vortex trajectories for this case. Again, the blue diamonds show the laboratory measurements vs. time, and the red squares show the corresponding numerical predictions. The solid and dashed lines joining the measurements and predictions show the depths of the vortices at unit values of T . Note the clockwise tilting of the line joining the vortex cores. The agreement is best at early times, which we expect due to using a 2-D numerical code. We also expect that a 3-D simulation of this case would produce a better agreement with the laboratory measurements at later times.

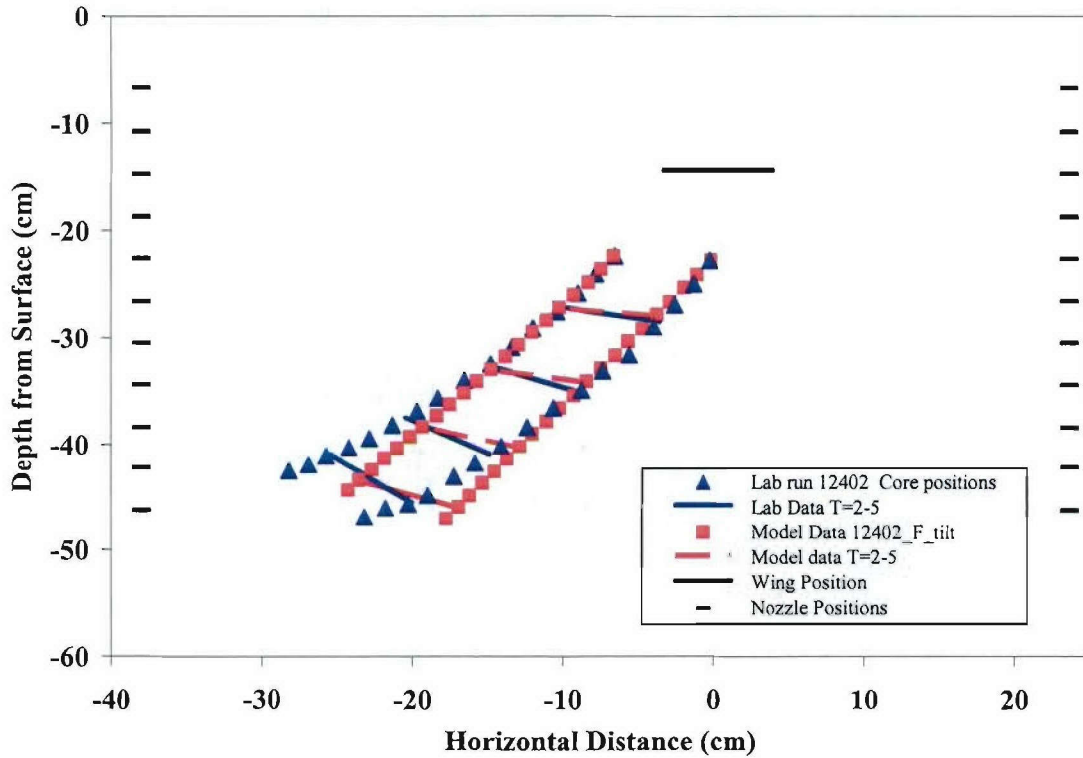


Figure 15. Vortex trajectories for the case with $V'' > 0$. The blue diamonds show the laboratory measurements vs. time, and the red squares show the corresponding numerical predictions using the laboratory measurements for wing depth, initial vortex descent velocity, initial vortex separation distance, and velocity (shear) profile. The solid black line at a depth of -15 cm shows the depth of the trailing edge of the wing that generates the vortex pair. The positions of the shear nozzles are shown as short solid lines on each side of the plot. The solid and dashed lines joining the measurements and predictions show the depths of the vortices at unit values of T . Note the clockwise tilting of the line joining the vortex cores.

Figure 16 quantifies the angle of tilt of the line joining the vortex cores for the $V'' > 0$ case. The blue triangles are the laboratory measurements, and the red squares are the predictions from the numerical model. For the case with $V'' > 0$, the tilt is clockwise.

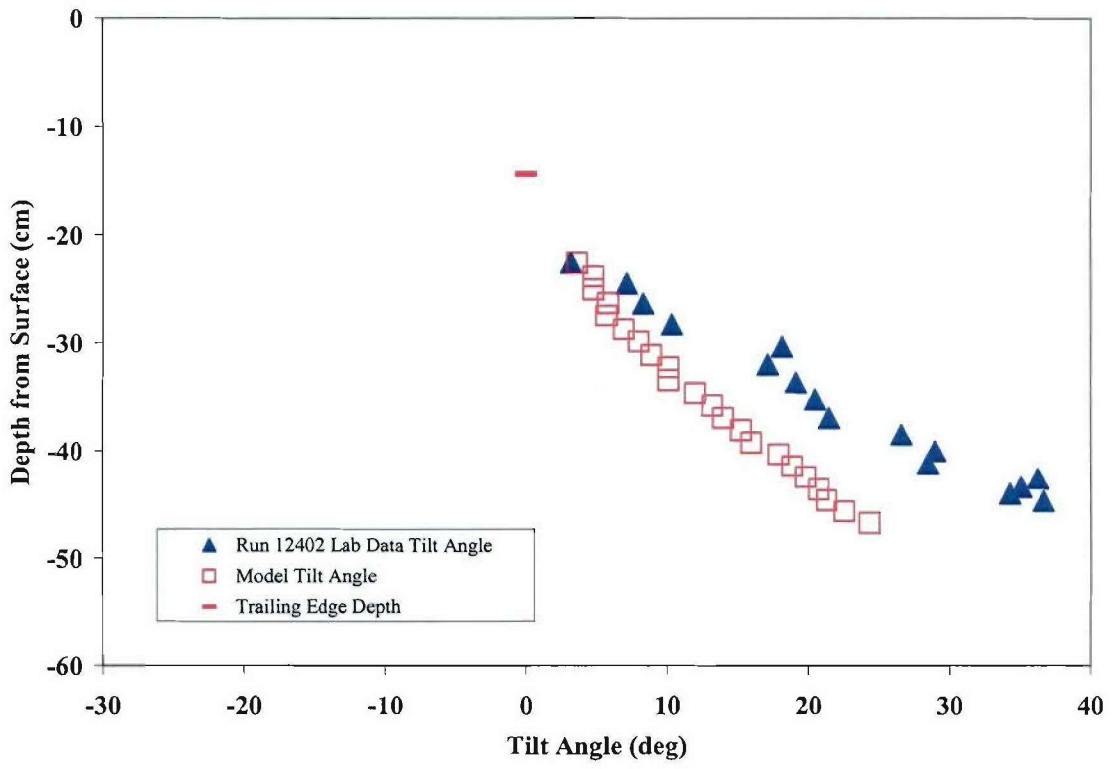


Figure 16. Measurements of the angle of tilt of the line joining the vortex cores for the $V'' > 0$ case. The blue triangles are the laboratory measurements, and the red squares are the predictions from the numerical model. For the case with $V'' > 0$, the tilt is clockwise.

5.3. Case with $V'' < 0$

Figure 17 shows the velocity profile measurements for the case for vortex evolution with $V'' < 0$. For this profile, we tried to maximize the vertical depth with $V'' < 0$, realizing that we had to bring the velocity profile back to zero at the bottom of the shear assembly in order to avoid large recirculation regions below the shear nozzles from disturbing the velocity profile. The triangles show the measured laboratory velocities as a function of depth below the surface. The curve through the measurements is a best fit to the data. The magenta line shows the part of the curve where $V'' > 0$, and the green lines show the parts where $V'' < 0$. The filled circle shows the starting depth of the laboratory wing generating the vortex pair. Note that this starting depth of 14 cm below the surface is within the region where $V'' < 0$ and that V'' remains negative until a depth of around 40 cm below the water surface.

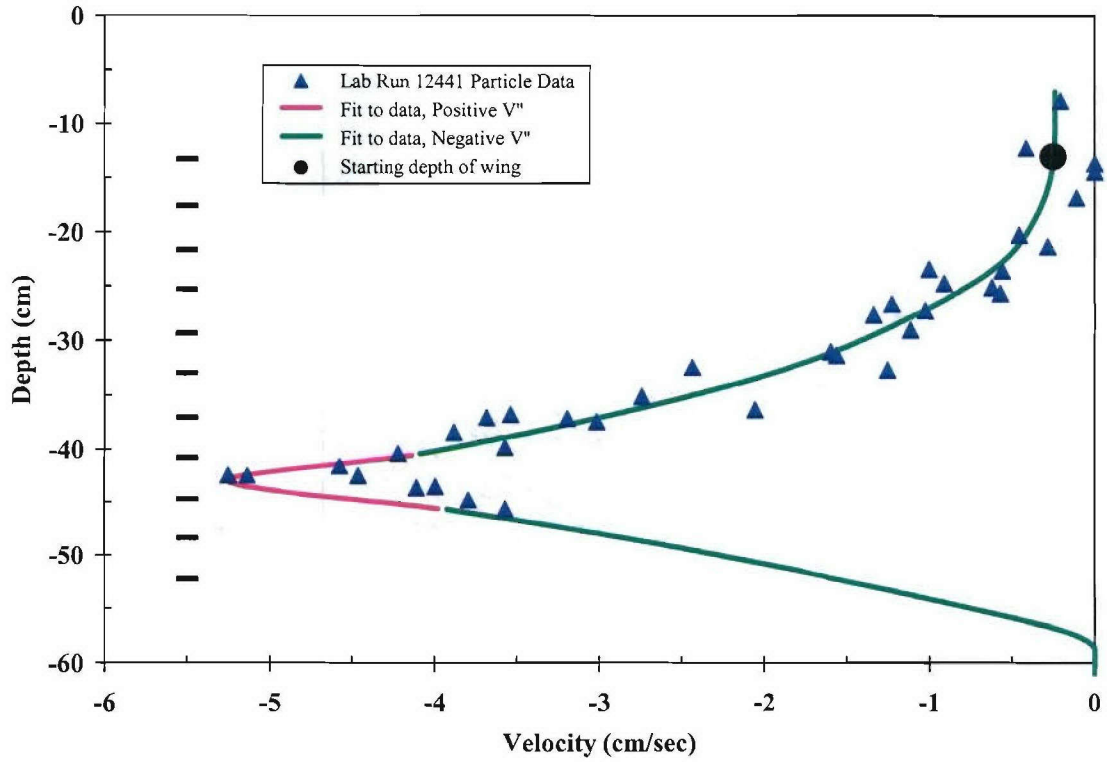


Figure 17. Velocity profile for the case for vortex evolution with $V'' < 0$. The triangles show the measured laboratory velocities as a function of depth below the surface. The curve through the measurements is a best fit to the data. The magenta line shows the part of the curve where $V'' > 0$, and the green lines show the parts where $V'' < 0$. The filled circle shows the starting depth of the laboratory wing generating the vortex pair. Note that this starting depth is within the region where $V'' < 0$.

Figure 18 shows vortex trajectories for the case with $V'' < 0$. The blue diamonds show the laboratory measurements vs. time, and the red squares show the corresponding numerical predictions using the laboratory measurements for wing depth, initial vortex descent velocity, initial vortex separation distance, and velocity (shear) profile. The solid black line at a depth of -14 cm shows the depth of the trailing edge of the wing that generates the vortex pair. The positions of the shear nozzles are shown as short solid lines on each side of the plot. The solid and dashed lines joining the measurements and predictions show the depths of the vortices at unit values of T . From eqn. (3), a velocity profile with $V'' < 0$ implies a counterclockwise tilt. Note the counterclockwise tilting of the line joining the vortex cores.

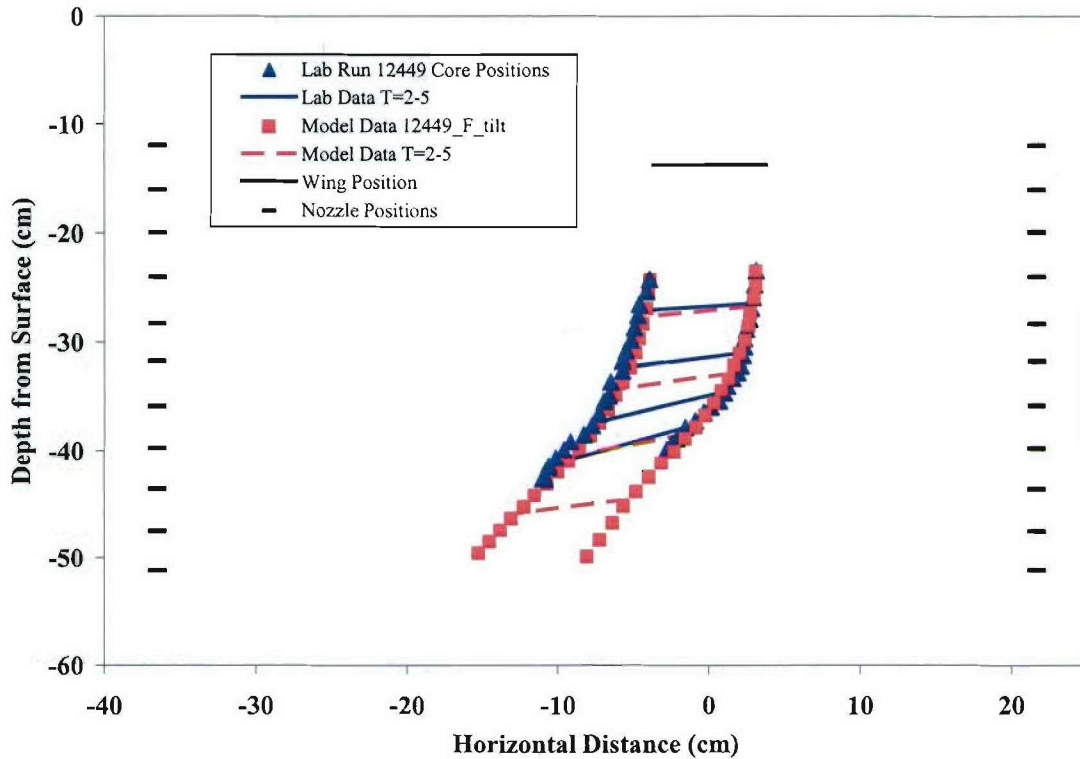


Figure 18. Vortex trajectories for the case with $V'' < 0$. The blue diamonds show the laboratory measurements vs. time, and the red squares show the corresponding numerical predictions using the laboratory measurements for wing depth, initial vortex descent velocity, initial vortex separation distance, and velocity (shear) profile. The solid black line at a depth of -14 cm shows the depth of the trailing edge of the wing that generates the vortex pair. The positions of the shear nozzles are shown as short solid lines on each side of the plot. The solid and dashed lines joining the measurements and predictions show the depths of the vortices at unit values of T . Note the counterclockwise tilting of the line joining the vortex cores.

Figure 19 shows measurements of the angle of tilt of the line joining the vortex cores for the $V'' < 0$ case. The blue triangles are the laboratory measurements, and the red squares are the predictions from the numerical model. Again, the agreement between the laboratory measurements and the numerical predictions is better initially, and the differences become larger as time progresses. We believe these differences are due primarily to our use of a 2-D code when the evolution is 3-D at later times. For the case with $V'' < 0$, Figure 19 shows that the tilt is counterclockwise, as expected. Note that the tilt begins to change directions around a depth of 40 cm below the surface. From Figure 17, this depth is where the velocity profile changes from $V'' < 0$ to $V'' > 0$. Near this depth, then, is where we would expect the tilt to reverse direction.

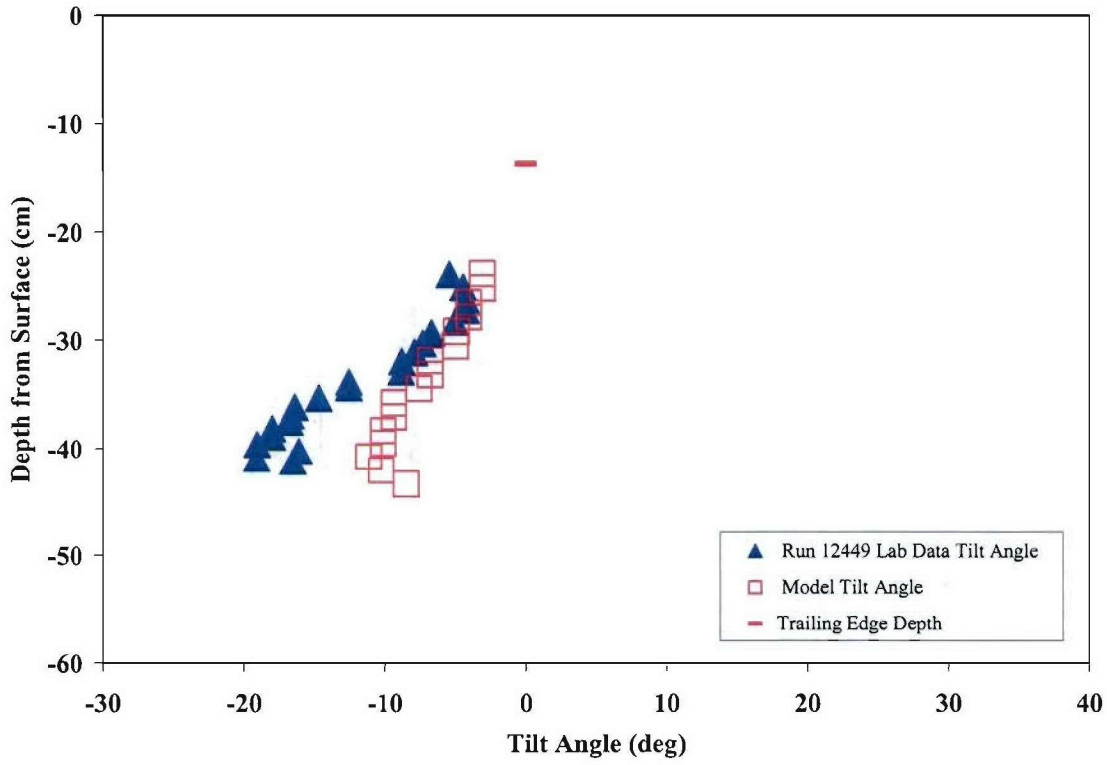


Figure 19. Measurements of the angle of tilt of the line joining the vortex cores for the $V'' < 0$ case. The blue triangles are the laboratory measurements, and the red squares are the predictions from the numerical model. For the case with $V'' < 0$, the tilt is counterclockwise.

5.4. Case with Mixed Shear

In Figure 17, the velocity profile below the peak was not well defined, since there were few shear nozzles below the depth of the maximum horizontal velocity. Yet, Figure 19 shows the start of a tilt reversal near where we thought the reversal should begin to be observed.

To attempt to see the reversal better, we devised a velocity profile like that shown in Figure 17, but with a velocity maximum occurring higher in depth, and with a better-defined profile below the peak velocity to bring the horizontal velocity back to zero at the bottom of the shear nozzles. The resulting velocity profile is shown in Figure 20. The filled circle shows the starting depth of the laboratory wing generating the vortex pair. Note that this starting depth is within the region where $V'' < 0$, but the profile shows a well defined region with $V'' > 0$ below this region, and there is a well defined region below the peak velocity region where $V'' < 0$ again.

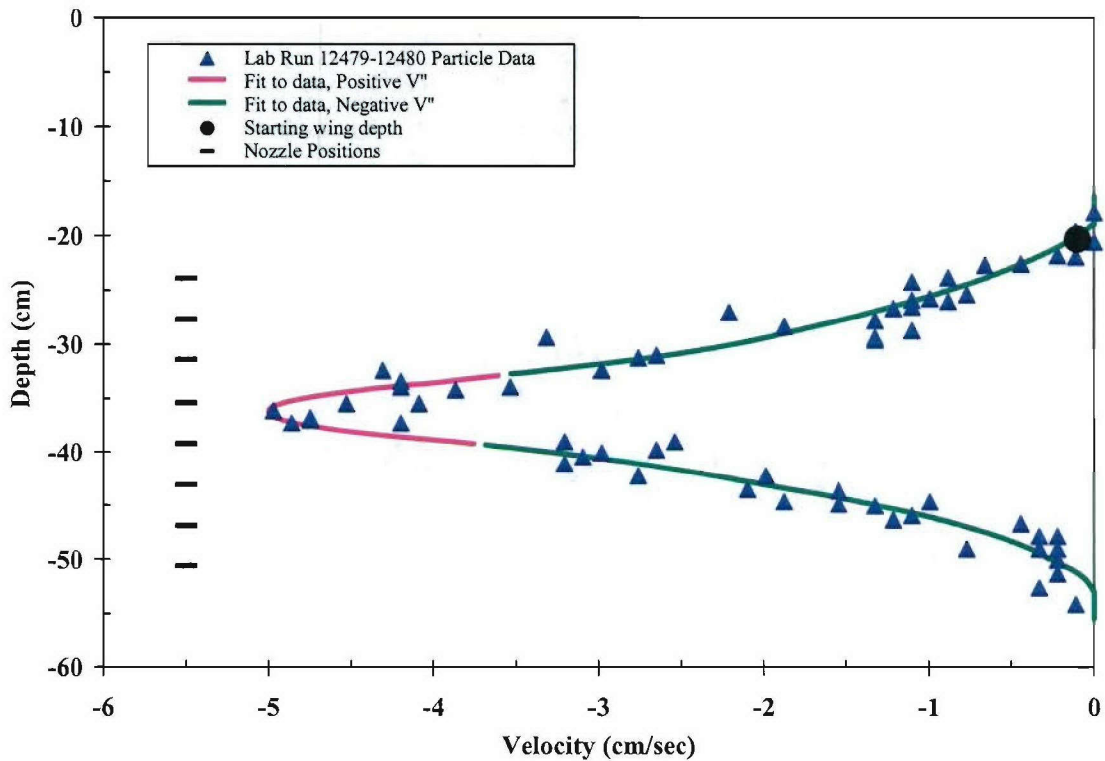


Figure 20. Velocity profile for the case with mixed shear ($V'' < 0$ and $V'' > 0$). The triangles show the measured laboratory velocities as a function of depth below the surface. The curve through the measurements is a best fit to the data. The magenta line shows the part of the curve where $V'' > 0$, and the green lines show the parts where $V'' < 0$. The filled circle shows the starting depth of the laboratory wing generating the vortex pair. Note that this starting depth is within the region where $V'' < 0$, but the profile shows a well-defined region with $V'' > 0$ below this region, and there is a well-defined region below the peak velocity region where $V'' < 0$ again.

Figure 21 shows vortex trajectories for the case with mixed shear. The blue diamonds show the laboratory measurements vs. time, and the red squares show the corresponding numerical predictions using the laboratory measurements for wing depth, initial vortex descent velocity, initial vortex separation distance, and velocity (shear) profile. The solid black line at a depth of -20 cm shows the depth of the trailing edge of the wing that generated the vortex pair. The positions of the shear nozzles are shown as short solid lines on each side of the plot. The solid and dashed lines joining the measurements and predictions show the depths of the vortices at unit values of T . From eqn. (3), we predict that, for the initial region where $V'' < 0$, we should see a counterclockwise tilt of the line joining the vortex cores. Below that region, in the region where we have the peak in horizontal velocity, where $V'' > 0$, we should see a clockwise tilt. Below the peak velocity region, where $V'' < 0$ again, the tilt should turn counterclockwise again. Figure 21 shows a counterclockwise tilting of the line joining

the vortex cores followed by a clockwise tilting. We do not see a second counterclockwise tilt (or a lessening of the clockwise tilt).

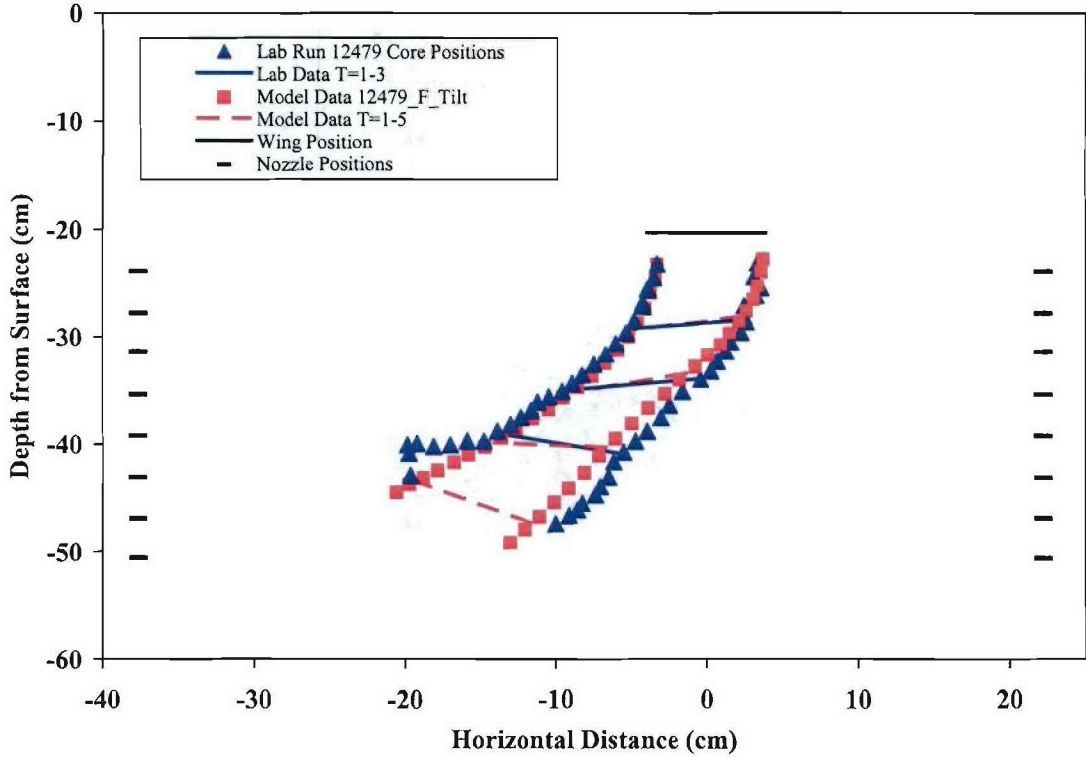


Figure 21. Vortex trajectories for the case with mixed shear. The blue diamonds show the laboratory measurements vs. time, and the red squares show the corresponding numerical predictions using the laboratory measurements for wing depth, initial vortex descent velocity, initial vortex separation distance, and velocity (shear) profile. The solid black line at a depth of -20 cm shows the depth of the trailing edge of the wing that generated the vortex pair. The positions of the shear nozzles are shown as short solid lines on each side of the plot. The solid and dashed lines joining the measurements and predictions show the depths of the vortices at unit values of T . Note the counterclockwise tilting of the line joining the vortex cores followed by a clockwise tilting.

Figure 22 quantifies the angle of tilt for the case with mixed shear. Again, the blue triangles are the laboratory measurements, and the red squares are the predictions from the numerical model. As in Figure 21, we do not see evidence of the second counterclockwise tilt. In order to explore this effect and to assess how a sharp change in the shear gradient affects vortex evolution, we explored the evolution of a vortex pair through a sharp jump in the shear gradient.

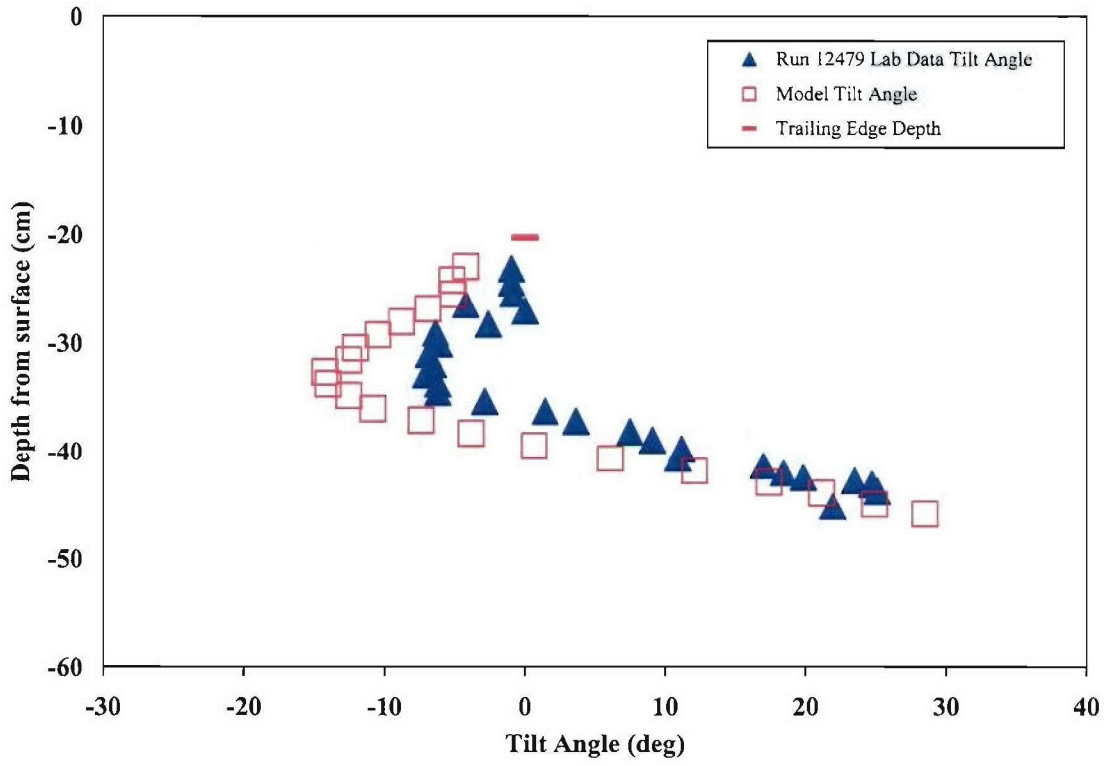


Figure 22. Measurements of the angle of tilt for the case with mixed shear. The blue triangles are the laboratory measurements, and the red squares are the predictions from the numerical model. For this case, we expect to see a counterclockwise tilt followed by a clockwise tilt followed by another counterclockwise tilt. We do not see the second counterclockwise tilt (or a lessening of the clockwise tilt).

5.5. Laboratory Measurements of Vortex Evolution through a Sharp Jump in Shear Gradient

Our previous laboratory experiments and numerical simulations used larger scale vertical gradients, with vertical scales on the order of the height of the vortex cell. Since many gradients in the ocean are sharp and of limited vertical extent (for example, the small-scale sheets and layers in the ocean), we want to assess how vortices evolve when they pass through gradients that are sharp vertically.

Figure 23 shows the velocity profile for the case with sharp vertical gradients of shear. The triangles show the measured laboratory velocities as a function of depth below the surface. The curve through the measurements is a best fit to the data. The filled circle shows the starting depth of the laboratory wing generating the vortex pair at a depth of -21 cm. This profile shows a region with zero gradient ($V'' = 0$) to a depth of around 25 cm, followed by a region with $V'' > 0$ to a depth of around 32 cm, followed by a region with $V'' < 0$ to a depth of around 39 cm, followed by a region with zero gradient

below. Thus, from eqn. (3), we would expect an initially clockwise tilt of the vortex cores as the cell migrates from the $V'' = 0$ region through the $V'' > 0$ region followed by a counterclockwise tilt as the cell migrates through the $V'' < 0$ region.

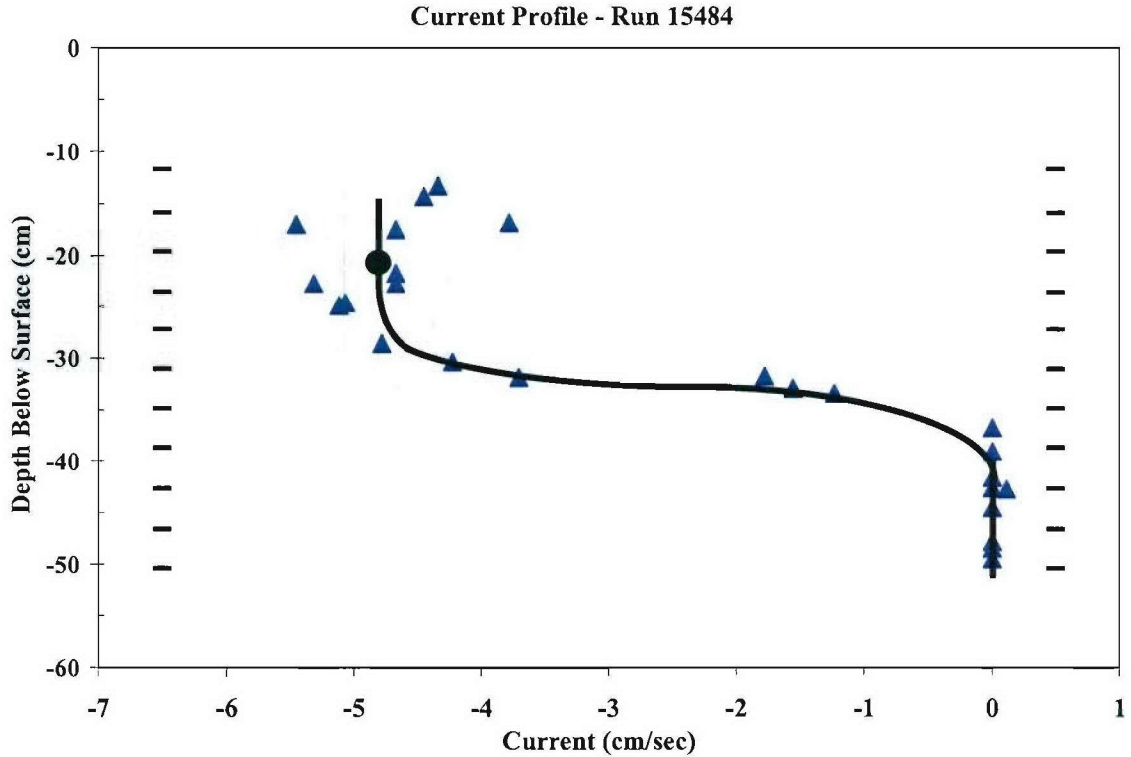


Figure 23. Velocity profile for the case with sharp vertical gradients of shear. The triangles show the measured laboratory velocities as a function of depth below the surface. The curve through the measurements is a best fit to the data. The filled circle shows the starting depth of the laboratory wing generating the vortex pair.

Based on the measured b_0 , the initial horizontal distance between the vortex cores, the vortex cell should be ~ 13 cm high. Placing such a cell on Figure 23 gives us Figure 24. We show Figure 24 to stress the point that the large variations in horizontal velocity are small vertically relative to the height of the vortex cell. We shall return to this point below.

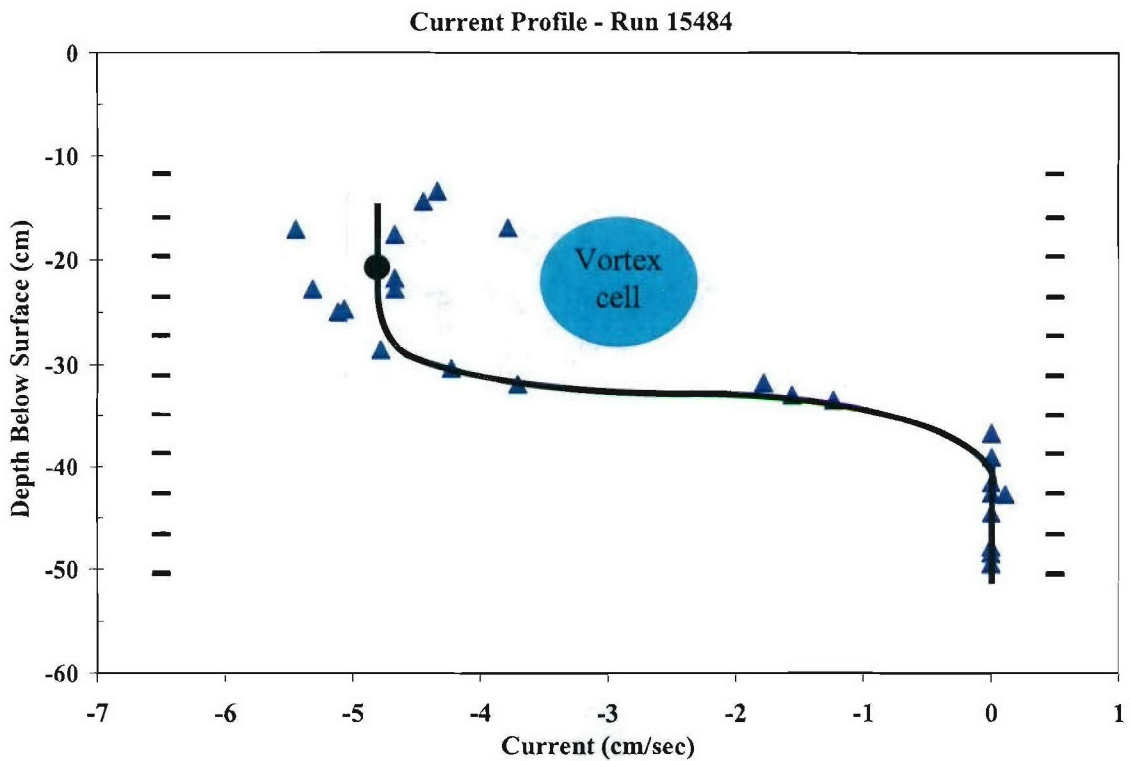


Figure 24. Similar to Figure 23 with the addition of the vortex cell.

Figure 25 shows laboratory measurements of vortex trajectories for the velocity profile shown in Figure 24. Figure 26 shows both the horizontal current measurements, shown in Figure 24, and the angle of tilt of the line joining the vortex cores for the case with sharp vertical gradients of shear. We have also superimposed the vortex cell from Figure 24 on this figure.

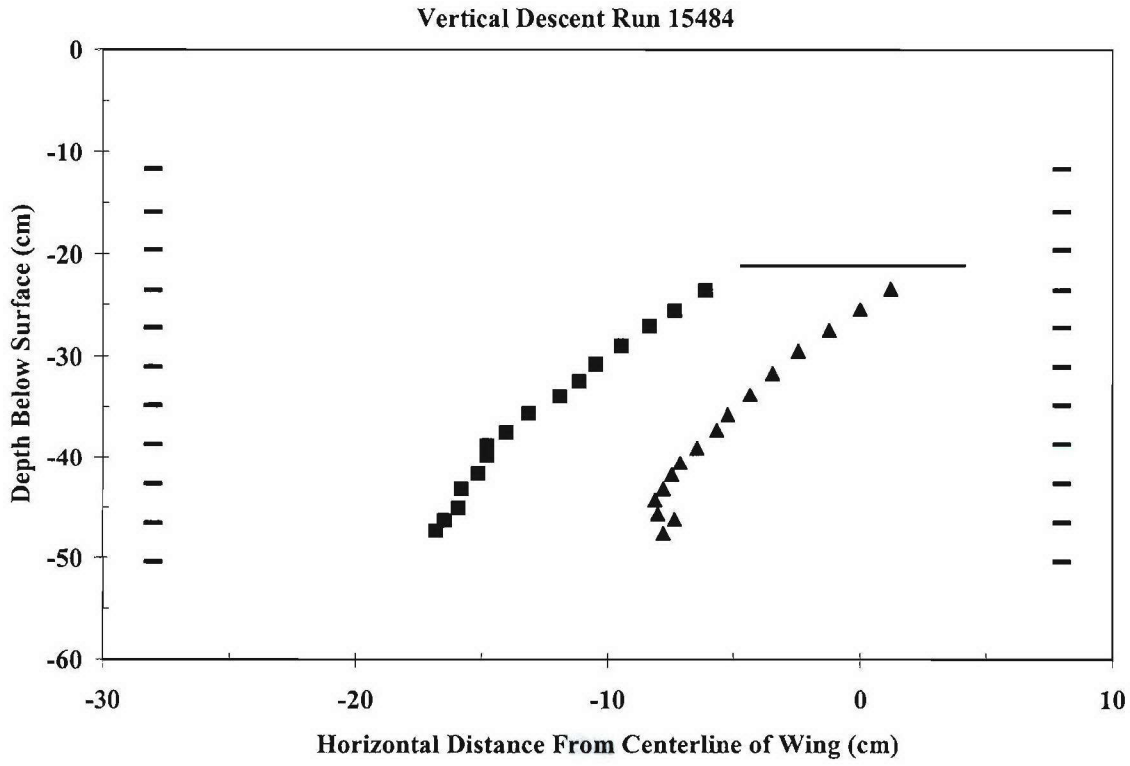


Figure 25. Laboratory measurements of vortex trajectories for the case with sharp vertical gradients of shear. The solid black line at a depth of -21 cm shows the depth of the trailing edge of the wing that generated the vortex pair. The positions of the shear nozzles are shown as short solid lines on each side of the plot.

Figure 26 shows several things of interest. We begin by noting that the tilt angle (the red circles in Figure 26) starts at zero at a depth of around 25 cm below the surface. The tilt angle then increases in the clockwise direction, starting at a depth around 26 cm, even though the shear gradient is near zero at that depth. The tilt angle continues to increase in the clockwise direction, as expected, reaching a maximum angle of around 13 degrees at a depth of around 38 cm. (Note that a depth of 38 cm is near where the shear gradient goes back to zero.) The tilt angle then reverses (becoming more counterclockwise) and comes back to zero slowly, reaching a value of zero at a depth of around 46 cm below the surface, where the shear gradient is definitely zero. Therefore, the first item to note in Figure 26 is that the tilt angle did return to zero, as we suspected but did not show in any of the above cases, particularly in the mixed shear case (Figure 22). The second item to note is that the tilt of the vortex cores appears to begin when the vortex cell first enters the region where the shear gradient is non-zero, and the tilt returns to zero when the vortex cell leaves the region where the shear gradient is non-zero. Thus, **the shear gradient affects the entire vortex cell, not just the vortex cores**. We suspected this effect since eqn. (3) is the result of integrating eqn. (2) over an area. The area, then, is essentially half the vortex cell.

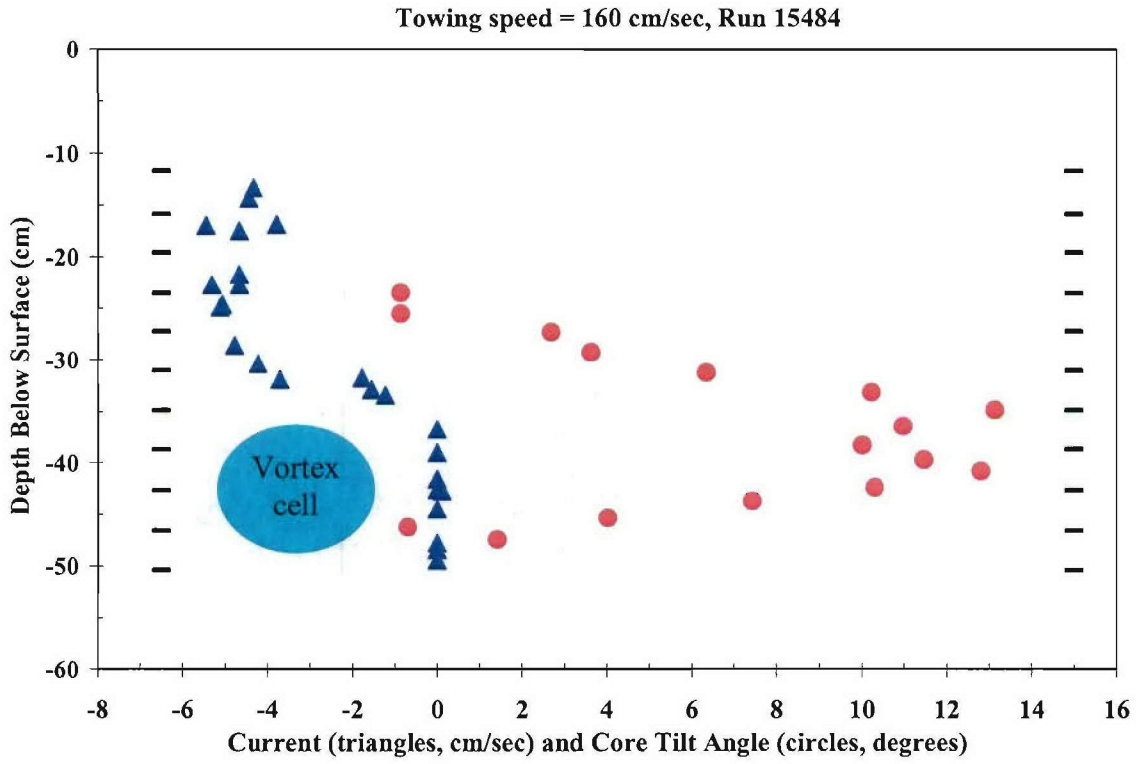


Figure 26. The angle of tilt of the vortex cores for the case with sharp vertical gradients of shear (red circles) along with the laboratory measurements of the velocity profile from Figure 23 (blue triangles). The vortex cell from Figure 24 has also been superimposed on the figure. The positions of the shear nozzles are shown as short solid lines on each side of the plot. Note that the tilt of the vortex cores appears to begin when the vortex cell first enters the region where the shear gradient is non-zero, and the tilt returns to zero when the vortex cell leaves the region where the shear gradient is non-zero. Thus, the shear gradient affects the entire vortex cell, not just the vortex cores.

The results for Figures 23 to 26 were obtained with a towing speed of 160 cm/sec. To explore the results of Figure 26 in a little more detail, we performed another experiment, using the same velocity profile as in Figure 23, but with a slower towing speed of 80 cm/sec. These results are shown in Figure 27. The angles of tilt for the towing speed of 160 cm/sec are shown as the red circles, and the angles of tilt for a towing speed of 80 cm/sec are shown as the black triangles.

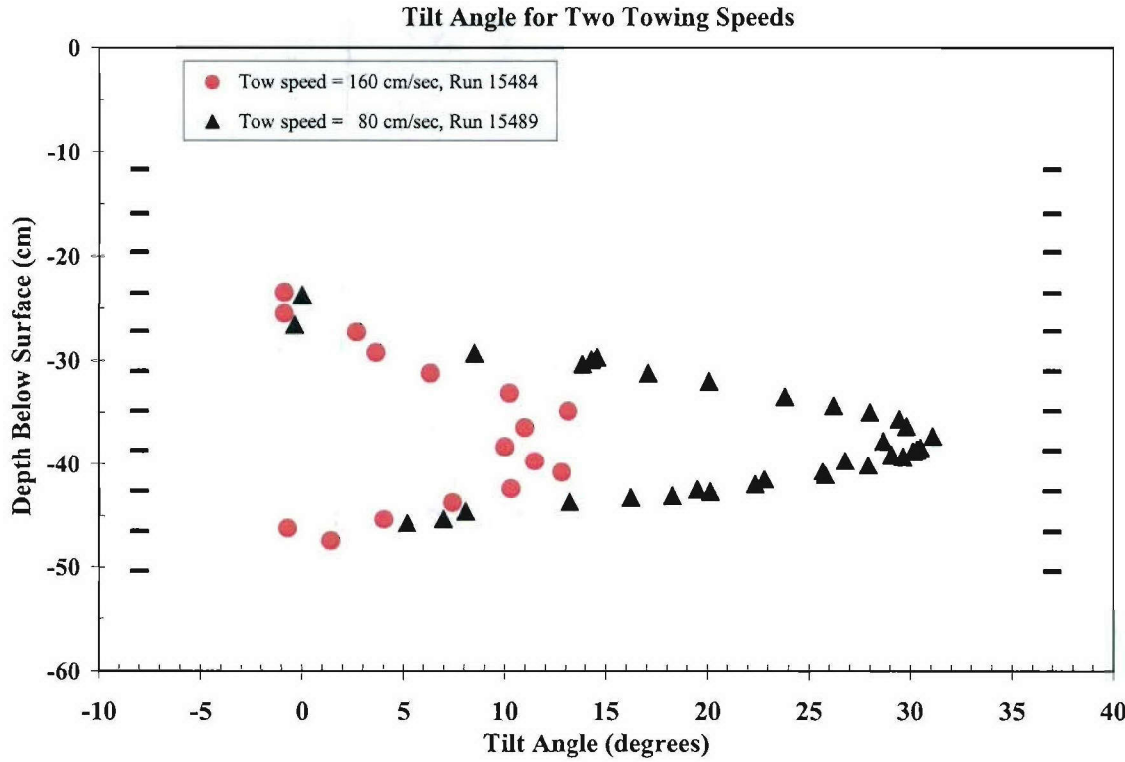


Figure 27. The angle of tilt of the vortex cores for the case with sharp vertical gradients of shear for a towing speed of 160 cm/sec (red circles; identical to those shown in Figure 26) and for a towing speed of 80 cm/sec (black triangles). In both cases, the velocity profile was that shown in Figure 23.

By towing the wing at a slower towing speed, we reduced the lift on the wing, reducing the initial circulation, Γ_o , and reducing V_o , the initial descent speed of the vortices. For reference,

$$\Gamma_o = 2\pi b_o V_o = L/\rho U b_o, \quad (4)$$

where L is the lift on the wing and U is the towing speed. Since the coefficient of lift is defined by

$$C_L = L/(0.5\rho U^2 (S^2/AR)), \quad (5)$$

where S is the wing span and AR is the Aspect Ratio. Using

$$C_L = \alpha (dC_L/d\alpha) \quad (6)$$

in (4) and (5), we get

$$V_o = (S^2/4\pi b_o^2 AR) (dC_L/d\alpha) \alpha U. \quad (7)$$

Since

$$(dC_L/d\alpha)/AR \approx \text{constant}, \quad (8)$$

and

$$S^2/4\pi b_o^2 = \text{constant for a given wing}, \quad (9)$$

eqn. (7) reduces to

$$V_o \approx \alpha U. \quad (10)$$

Equation 10 tells us that the initial descent speed, V_o , is dependent on the angle of attack and the towing speed, U . In Figure 27, the angle of attack was held constant, but the towing speed was varied from 160 cm/sec to 80 cm/sec. Thus, V_o varied by roughly a factor of 2. (Laboratory measurements for these flows showed that V_o was ~ 6.51 cm/sec for the 160 cm/sec runs and ~ 3.45 cm/sec for the 80 cm/sec runs, a factor of 1.9.)

In Figure 27, note that the tilt angles for both runs start from zero at nearly the same depth, have a maximum tilt at nearly the same depth, and come back to zero at around the same depth. Thus, the depths where the vortex cores begin and end their tilt is not dependent on the towing speed, the lift, or V_o . However, the magnitude of the tilt is dependent on these quantities. Figure 27 shows that, when the vortex cell passes through the shear gradient slower ($U = 80$ cm/sec), the tilt of the vortex cores reaches a maximum angle of around 31 degrees. When the vortex cell passes through the shear gradient faster ($U = 160$ cm/sec), the tilt of the vortex cores reaches a maximum angle of around 13 degrees. Thus, the tilt of the vortex cores is dependent on the speed the vortex cell moves through the shear gradient.

5.6. 3-D Numerical Simulations

In order to assess the importance of three-dimensional effects of vortices migrating through a shear gradient, we performed three 3-D numerical simulations: (1) With no ambient turbulence and no ambient shear, (2) With ambient turbulence but no ambient shear, and (3) With ambient turbulence and with ambient shear. When possible, we compared the predictions from the numerical simulations to laboratory measurements. These laboratory measurements were not performed as part of this study. However, these measurements are summarized below since we will compare the numerical predictions to these laboratory measurements.

5.6.1. Previous Laboratory Measurements

Under previous funding, NWRA performed laboratory studies to investigate how a vortex pair evolved with ambient turbulence (Delisi, 2006). The laboratory experiments were performed by towing a grid down a tank filled with unstratified water and following the grid with a wing generating lift at an angle of attack. The resulting trailing wake vortices from the wing were observed using dye and hot film probes.

Three different grids were used in the study. The mesh size of the grids was varied to explore how eddy size affected the evolution of the vortices. The grids had square meshes of 1.9 cm, 5.7 cm, and 9.5 cm. The grids covered nearly the entire cross section of the towing tank, except for approximately 20 cm at the bottom of the tank. The grids were towed at 50 cm/sec.

A typical experiment started with the grid being towed down the tank. We then towed the wing down the tank so that the wing would arrive in the test section a certain number of seconds after the grid had passed the center of the test section. The time difference between when the grid and the wing passed by the test section varied between 4 and 20 seconds. We followed the evolution of the trailing vortices using dye in the vortex cores. Video cameras on the side and top of the tank were used to document the wake evolution.

We note that, with this method of generating ambient turbulence, the turbulence in the test section will decrease in intensity with time. In this study, we measured the turbulence intensity as a function of distance behind the grid with hot film probes, and we used the decay as a function of time in the test section. The turbulence intensities stated here are an average value between the time of passage of the wing (and the generation of the vortices) and the time the vortices link into vortex rings.

As the trailing vortices evolve behind the wing, Crow instability develops, until the line vortices finally link into three-dimensional (3-D) rings (see, e.g., Robins and Delisi, 1997 and Delisi and Robins, 2000). We measured the peak-to-peak amplitudes of this instability as a function of time using cameras looking into the side of the towing tank (see Figure 2 in Delisi and Robins, 2000). Figure 28 shows these peak-to-peak vertical amplitude measurements as a function of nondimensional time, T . We measured V_o by measuring the vertical descent of the vortices from cameras looking into the test section from the side of the tank, and we measured b_o from cameras looking into the test section from the top of the tank. In Figure 28, the black squares show measurements from two runs with no grid, and, hence, with little ambient turbulence. The larger symbols for each run show the times of vortex linking, when the vortices evolve from two-dimensional (2-D) line vortices into 3-D vortex rings. For these two runs, linking occurred at $T = 6.27$ and 6.87 , with nondimensional amplitudes of around 1. The remaining measurements in Figure 28 were obtained at various distances, and, hence, varying turbulence intensities, behind the grid. For these runs, ε^* is the normalized turbulent dissipation rate defined as $(\varepsilon b_o)^{1/3}/V_o$, where ε is the turbulent dissipation rate measured behind the grid. Here, ε^* is the average value between when the wing passed,

and the vortices were generated, and the time of linking of the 2-D vortices into 3-D vortex rings. Figure 28 shows that, as the ambient turbulence increases, the vortices link sooner. Similar results were shown by Sarpkaya and Daly (1987).

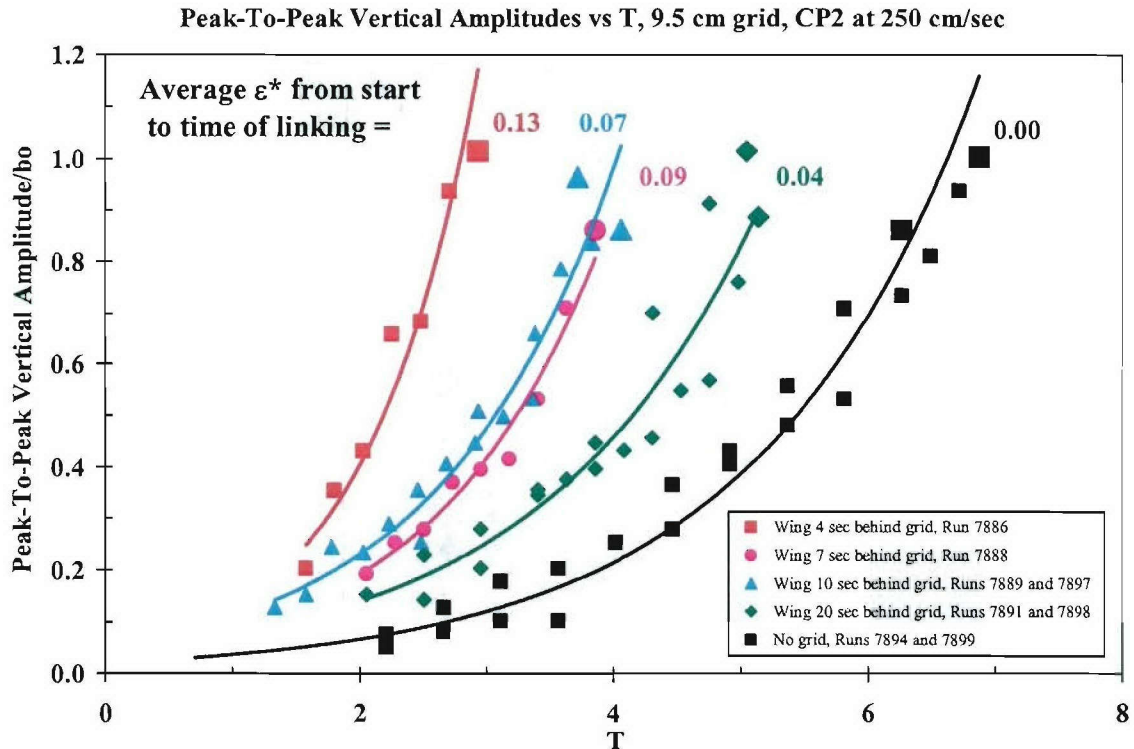


Figure 28. Laboratory measurements of the peak-to-peak vertical amplitude of two-dimensional line vortices generated from a wing as a function of nondimensional time for runs with varying amounts of ambient turbulence. T is nondimensional time, and ϵ^* is the normalized turbulent dissipation rate averaged between the time of passage of the wing and the time of vortex linking. The larger symbols for each condition show the times of vortex linking, when the vortices evolve from two-dimensional (2-D) line vortices into 3-D vortex rings. These laboratory measurements show that, as the ambient turbulence increase, the vortices link sooner. From Delisi (2006).

What was new in these results is not what happens before vortex linking, but what happens to the vortices after linking. In these previous studies, we showed that there was no significant difference in the vertical migration between runs with ambient turbulence and runs without ambient turbulence. Thus, ambient turbulence has a significant effect on the time vortices evolve from 2-D lines into 3-D rings, but does not have a significant effect on vortex decay. However, here, we shall only be concerned with the laboratory measurements shown in Figure 28, which show the effect of the ambient turbulence on the time to form 3-D rings.

5.6.2. 3-D Numerical Simulations

Three 3-D numerical simulations were performed. The first of these simulations was performed in a flow with no ambient turbulence and no ambient shear, and with the laboratory conditions of the black squares in Figure 28. The results of this simulation are shown in Figure 29. It can be seen that the results of amplitude growth for the no turbulence and no shear numerical simulation agree very well with the laboratory data (the gray squares with $\varepsilon^* = 0.00$ in Figure 29). For this case, we adjusted the initial axial perturbations of the superimposed vortices in order to obtain the good agreement shown here. We found that we needed to set the perturbation amplitude of each vortex component to 0.05^*b_o , in order to obtain the agreement shown. (One way to think about this perturbation amplitude is that it represents the oscillations induced by the laboratory process required to generate the vortices.) We will treat the no turbulence, no shear case as the baseline for our other two simulations.

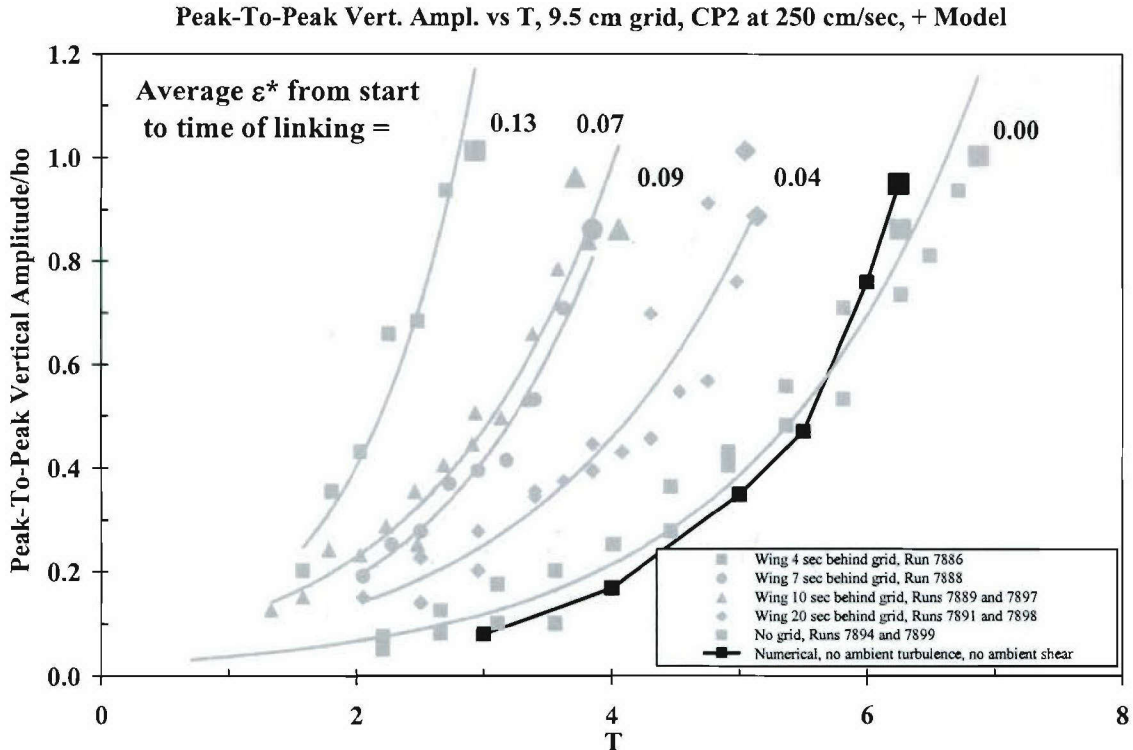


Figure 29. Similar to Figure 28 with the addition of the 3-D numerical predictions for the case with no ambient turbulence and no ambient shear (black squares). In this figure, all the laboratory data are shown as gray symbols.

For the second simulation, we added ambient turbulence to the baseline case. The initial level of ambient turbulence was chosen so that the average ε^* over the run was close to the laboratory case, where the average laboratory ε^* was 0.13 (c.f., Figure 28). It

turned out for the simulation that the average ϵ^* was 0.14. The results from this simulation are shown as the pink triangles in Figure 30. Here, the simulation results do not overlay the laboratory case with $\epsilon^* = 0.13$ case, but agree well with the laboratory cases when the average ϵ^* in the laboratory was in the range 0.07 to 0.09. One possibility for this result is that the initial perturbation in the laboratory due to the vortex generation process may have been greater in the case with significant ambient turbulence than for the zero turbulence case. Thus, we suspect that, if the initial perturbation in the numerical simulation were $0.1b_0$ instead of $0.05b_0$, the simulation results would have agreed more closely with the laboratory data for the $\epsilon^* = 0.13$ case.

For the third simulation, we added a current profile to the above case with ambient turbulence. The profile we added was that in Figure 14, with $V'' > 0$. For this case, we started the numerical simulation at a distance of about one b_0 above the maximum of the jet. In Figures 15 and 16, we saw a clockwise tilt to the vortex cores, which we expected from eqn. (3). The results of the 3-D simulation are shown as the red circles on Figure 30. This figure shows that adding shear to the second simulation delays the linking of the line vortices into 3-D rings (from the large, pink triangle at $T = 4.25$ for the case with ambient turbulence but no shear to the large, red circle at $T = 5.75$ for the case with ambient turbulence and ambient shear).

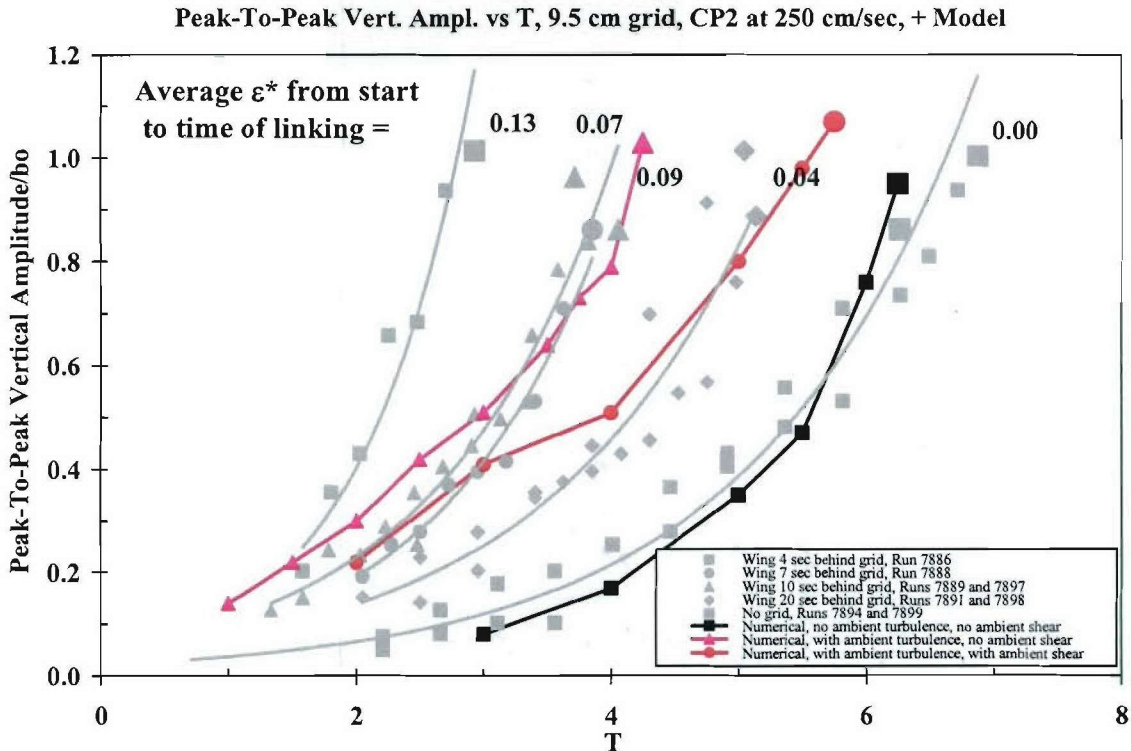


Figure 30. Similar to Figure 29 with the addition of the 3-D numerical predictions for the case with ambient turbulence and no ambient shear (pink triangles) and the case with ambient turbulence and ambient shear (red circles). In this figure, all the laboratory data are shown as gray symbols.

Figure 31 shows an H vs T plot for the three 3-D numerical simulations, where $H = h/b_0$ and h is dimensional depth. The numerical predictions for the case with no ambient turbulence and no shear are shown as the black squares, the predictions for the case with ambient turbulence but no shear are shown with the pink triangles, and the predictions for the case with ambient turbulence and with shear are shown with the red circles. For all cases, the larger symbols show the times of vortex linking, when the vortices evolve from 2-D line vortices into 3-D vortex rings. Note how the addition of turbulence to the no turbulence case does not affect the descent of the vortices (comparing the triangles to the squares). This similarity in vertical descent is consistent with the laboratory measurements. Note also, that adding shear to the case with ambient turbulence reduces the vertical migration and also delays linking (comparing the circles to the triangles). Thus, the effect of the shear is to delay the onset of linking and to simultaneously reduce the vertical migration of the vortices.

NWRA 3-D Numerical Simulations

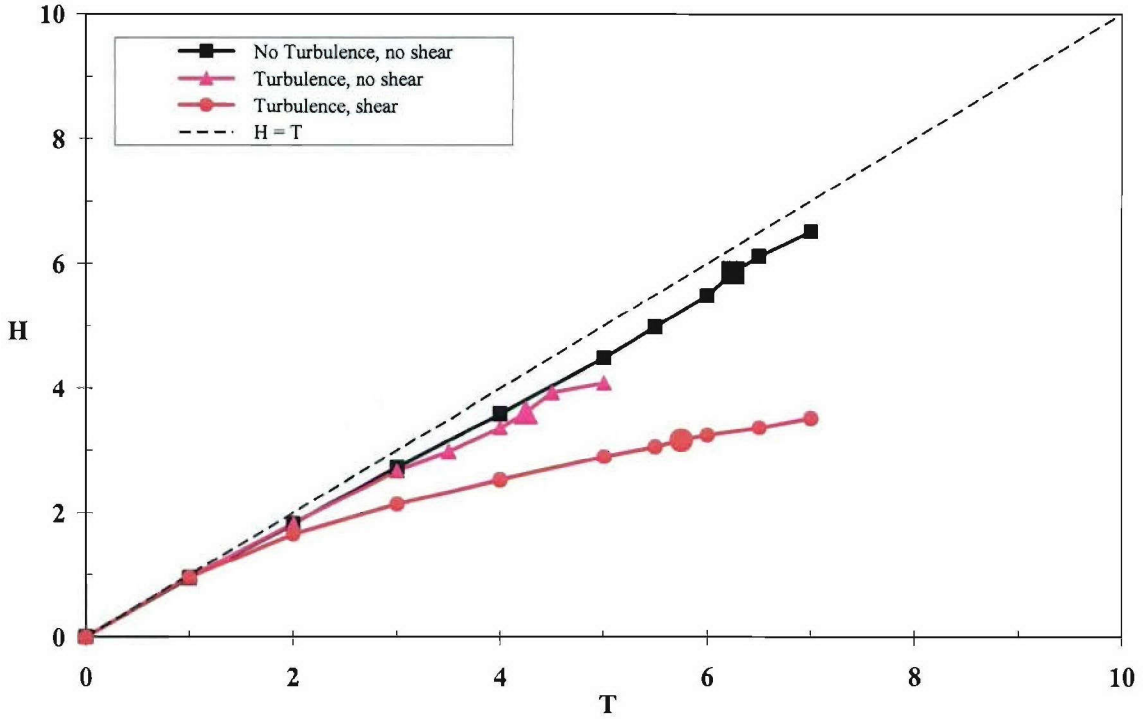


Figure 31. H vs T plot for the three 3-D numerical simulations. The numerical predictions for the case with no ambient turbulence and no shear are shown with the black squares. The predictions for the case with ambient turbulence but no shear are shown with the pink triangles. The predictions for the case with ambient turbulence and with shear are shown with the red circles. In all runs, the larger symbols for each case show the times of vortex linking, when the vortices evolve from 2-D line vortices into 3-D vortex rings. Note how the addition of turbulence to the no turbulence case does not affect the descent of the vortices (comparing the triangles to the squares). This similarity in vertical descent is consistent with the laboratory measurements. Note also, that adding shear to the case with ambient turbulence reduces the vertical migration and also delays linking (comparing the circles to the triangles). Thus, the effect of the shear is to delay the onset of linking and to reduce the vertical migration of the vortices.

Visualizations of frames from these three numerical simulations are shown in Figure 32. In this figure, the top row shows the flow at $T = 2$, the second row at $T = 3$, the third row at $T = 4$, and the bottom row at $T = 5$. Also, the left column shows plots for the case with no ambient turbulence and no ambient shear, the middle column shows plots for the case with ambient turbulence but no ambient shear, and the right column shows plots for the case with ambient turbulence and with ambient shear. For all plots, the vortices are shown in the middle of the plot. On the left-most wall of the box is a side projection of the vortices, as if being lit from the right hand side, and on the bottom of the box is a top projection of the vortices, as if being lit from the top.

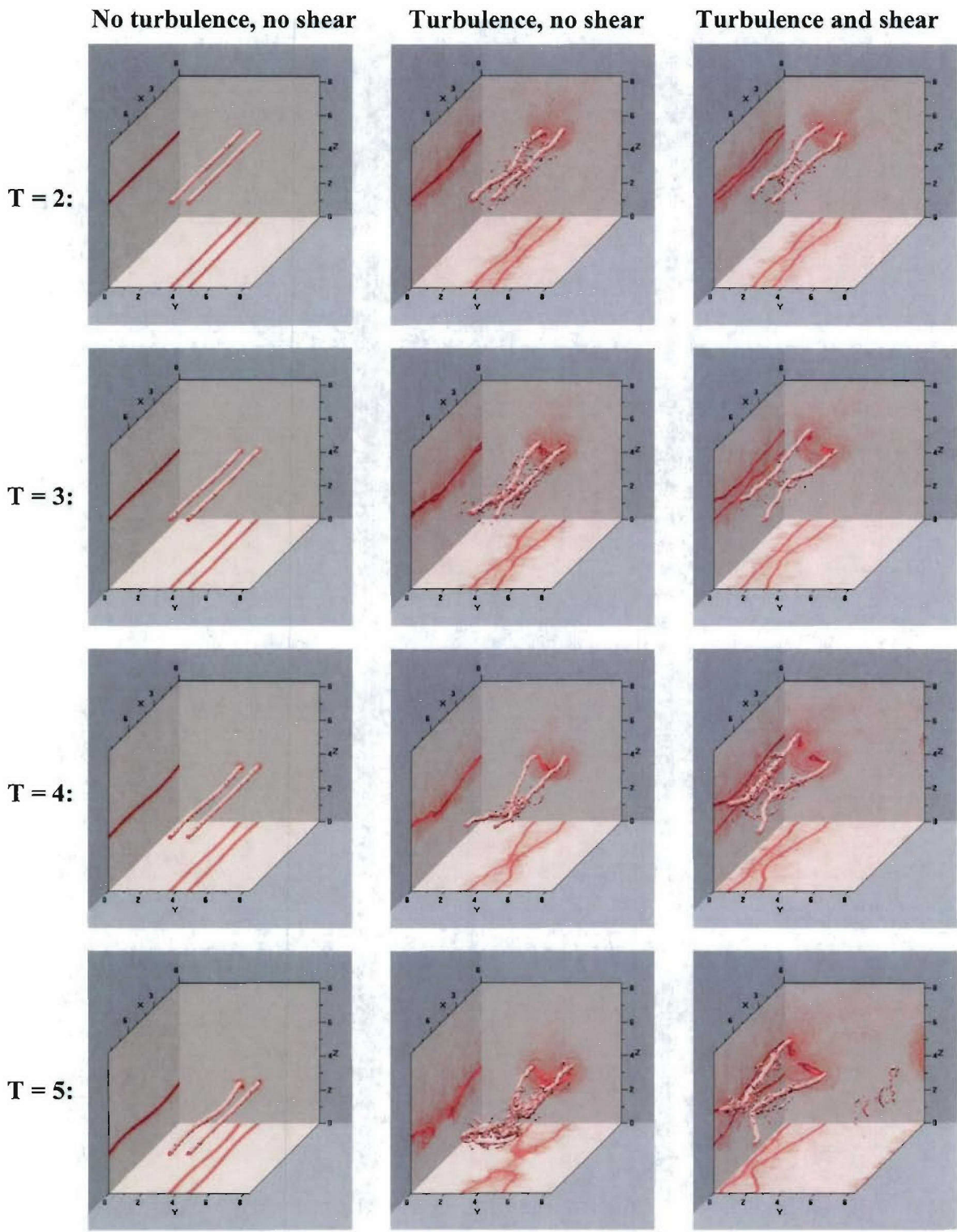


Figure 32. Numerical model results for the no turbulence no shear case (left column), turbulence, no shear case (middle column) and turbulence and shear case (right column) for $T = 2$ (top row), $T = 3$ (second row), $T = 4$ (third row) and $T = 5$ (bottom row).

We begin our discussion of Figure 32 for the case with no ambient turbulence and no ambient shear (the left-most column in Figure 32). Following the evolution of the vortices from the top ($T = 2$) to the bottom ($T = 5$), we see that the vortex pair descends downward, at a nearly constant rate, with some three-dimensionality appearing at $T = 4$, and more three-dimensionality showing at $T = 5$, as the vortices exhibit Crow instability and begin to evolve into 3-D rings.

For the middle column, the case with ambient turbulence but no ambient shear, the vortices at $T = 2$ already exhibit significant three-dimensionality, presumably due to the ambient turbulence which moves parts of the line vortices around asymmetrically, and promotes the growth of Crow instability. By $T = 4$, the vortices have very nearly linked (see the projection on the bottom floor of the numerical box), and the vortices have linked and formed rings by $T = 5$. (This linking is consistent with Figure 30, where we saw linking at $T = 4.25$.)

For the right hand column in Figure 32, the case with ambient turbulence and ambient shear, at $T = 2$ we see three-dimensionality similar to that shown in the middle column, but we also see a significant tilting of the vortex cores (see the projection on the left-most wall of the numerical box). As time continues for this case, the tilt becomes more prominent and the vortices move sideways in the numerical box, due to the movement of the vortices by the horizontal currents. At $T = 5$, note that the vortices have not yet linked, even though the vortices without the ambient shear (middle column) have linked. Also, note the decreased vertical descent for the case with ambient turbulence and ambient shear at $T = 5$.

6. Summary

This study has shown several new and important results for the evolution of a vortex pair in a realistic environment. These new results are the following:

1. The evolution of a vortex pair is affected by small-scale and large-scale vertical gradients in shear (where shear is defined as a change in the horizontal velocity profile with depth).
2. Laboratory experiments and numerical simulations based on the laboratory conditions both show a tilt of the line joining the vortex cores when the shear gradient is non-zero ($V'' \neq 0$). Equation (3) can be used to predict this tilt.
3. The stronger the shear gradient, the larger the vortex tilt.
4. The slower the vertical migration speed of the vortex pair through the shear gradient, the larger the vortex tilt.
5. A shear gradient delays vortex linking.

6. A shear gradient results in a decreased vertical descent of the vortex pair.

For the Navy, these results imply the following:

- a. Vertical shear appears to be an important effect for vortex evolution in the ocean. It is probable that the vortex-tilting phenomenon observed in this study, along with the simultaneous decrease in vertical descent, may have an important effect on vortex migration in the ocean. An assessment of the magnitude of this effect on vortex evolution in the ocean should be performed using measured ocean profiles.
- b. Although the effects of ambient stratification, ambient turbulence, and ambient shear have been assessed, we do not have an assessment of the combined effects of ambient stratification, ambient turbulence, and ambient shear. In other words, we do not know how a vortex pair will evolve in an environment when ambient stratification, turbulence, and shear are all present. As one example, we have shown that ambient shear delays vortex linking (Figures 30, 31, and 32). We also know that ambient turbulence promotes vortex linking (Figures 28, 30, 31, and 32). But, in a flow with both ambient turbulence and ambient shear, we do not yet know the parameters which govern vortex linking. Since these effects are nonlinear, additional studies should be performed to result in better ocean predictions.

References:

- Delisi, D.P., 2006. Laboratory Measurements of the Effect of Ambient Turbulence on Trailing Vortex Evolution, to be presented at the 44th AIAA Aerospace Sciences Meeting, Reno, January.
- Delisi, D.P. and R.E. Robins, 2000. Short-scale instabilities in trailing wake vortices in a stratified fluid, *AIAA J.*, **38**, 1916-1923.
- de Bruyn Kops, S.M. and J.J. Riley, 1998. Direct numerical simulation of laboratory experiments in isotropic turbulence, *Phys. Fluids*, **10**(9), 2125-2127.
- Holzäpfel, F., 2004. Adjustment of subgrid-scale parameterizations to strong streamline curvature, *AIAA J.*, **42**, 1369-1377.
- Robins, R.E. and D.P. Delisi, 1997. Numerical simulations of three-dimensional trailing vortex evolution, *AIAA J.*, **35**, 1552-1555.
- Robins, R.E. and D.P. Delisi, 1998. Numerical simulation of three-dimensional trailing vortex evolution in stratified fluid, *AIAA J.*, **36**, 981-985.
- Sarpkaya, T. and J.J. Daly, 1987. Effect of ambient turbulence on trailing vortices, *J. Aircraft*, **24**, 399-404.